University of Naples “FEDERICO II”

PhD in *Industrial Product and Process Engineering*
Department of Chemical, Materials and Production Engineering

and

University of STRASBOURG
PhD in *Physics and Physical Chemistry*
Charles Sadron Institute, ICS- UPR 22 CNRS

Development of composite polymeric nanoparticles and their application to optical sensors

Candidate: Chiara TADDEI

PhD Supervisor: Prof. Christophe SERRA and Prof. Michele GIORDANO
PhD Coordinator: Prof. Giuseppe MENSITIERI

Acknowledgments

A great thanks goes to the Institute for Polymeric Materials, Composites and Biomaterials of Naples, where I have carried out most of my doctoral research activities. I would also like to acknowledge Prof. Giuseppe Mensitieri and Paola Desidery for their support and the contribution in the development of my thesis project.

Furthermore, I would like to express my gratitude to Prof. Christophe Serra for the collaboration, and for allowing me to spend part of my doctoral activities in his lab at the Institute Charles Sadron in Strasbourg.

Table of contents

List of Figures iii
List of Tables vii
Abbreviations viii

Introduction 1
  1.1. Motivation 1
  1.2. Thesis organization 2

Background Literature 5
  2.1 Photonic Crystal 5
  2.2 Responsive Photonic Crystal 13
  2.2.1 ThermoResponsive Photonic Crystals 14
  2.2.2 Chemically Responsive Photonic Crystals 15
  2.2.3 Mechanically Responsive Photonic Crystals 17
  2.2.4 Magnetically Responsive Photonic Crystals 18
  2.3 Biosensor based on Photonic Crystals 22
  2.4 The Optical Fiber Tip Sensors 24

Self-assembled colloidal photonic crystal on the fiber optic tip and its application 31
  3.1 Abstract 31
  3.2 Materials and Procedure 32
  3.3 Spectral Characterization 33
  3.4 Numerical Analysis 35
  3.5 Humidity sensitive photonic crystal hydrogel 50
  3.5.1 Materials and Procedure 50
  3.5.2 Morphology Characterization 51
  3.5.2 Relative humidity measurements 53
  3.6 Conclusions 57

Label-free optical biosensing at sub-femtomolar detection limits 59
  4.1 Abstract 59
  4.2 Materials and Procedure 60
  4.3 Spectral Characterization 61
  4.4 Fiber functionalization and dose response measurements 63
  4.5 Results and Discussion 64

Table of Contents

4.6 Conclusions 68

Magnetic photonic crystal for high sensitivity optical sensor 69
5.1 Abstract 69
5.2 Materials and Procedure 73
5.3 Morphology Characterization 80
5.5 Magnetic analysis 89
5.5 Conclusions 90

Conclusions and perspectives 91
6.1 Conlusions 91
6.2 Future perspectives 92

Appendix I - Characterization Techniques 94
I. Scanning Electron Microscopy (SEM) 94
II. Transmission Electron Microscopy (TEM) 96
III. Thermogravimetric Analysis (TGA) 97
IV. Optoelectronic Setup 97
V Magnetic Measurements 99
References 101

List of Figures

Figure 2. 1. Schematic illustration of 1D, 2D and 3D periodicity of photonic crystals structure. Adapted from Ref [3]. 6
Figure 2. 2. Vertical deposition: a) Original setup; b) combination with slow lifting of the sample; c) assumed processes. (Picture parts are adapted from Ref. [20]) [6] .. 9
Figure 2. 3. Photograph of the wings of Morpho Menelaus butterfly. Inset, the right wing of the butterfly is wetted with ethanol. The change in the refractive index induces the color change from blue to green. From Ref [6]. 10
Figure 2. 4.Simplified scheme of light reflection from ordered spheres. 11
Figure 2. 5.Temperature dependence of the reflection spectrum of porous NIPAM gel built with a colloidal crystal template composed of silica nanoparticles (d=210 nm). From Ref. [33]... 15
Figure 2. 6. a) SEM image of the cross section of an eight-layer Bragg reflector made of silica and titania nanoparticles deposited alternately on the substarte. b) Reflection of the Bragg reflector infiltrated with water, ethylene glycol and chlorobenzene. From Ref. [35].. 16
Figure 2. 7. (a) and (b) Typical microscope images of PAAm–P(St–MMA–AA) PC hydrogel (a) dry state, (b) wet state. (c) top view of the SEM image of PAAm–P(St–MMA–AA) PC hydrogel. (d) and (e) Reversible changes of the color/stopband of the PAAm–P(St–MMA–AA) PC hydrogel with relative humidity. (d) Photographs of the as-prepared PC hydrogel corresponding to different relative humidities (e) Reversible conversion of the stopband position of the PC hydrogel by alternately exposing to increasing and decreasing relative humidity conditions. From Ref. [37]. 17
Figure 2. 8. a) Reversible tuning by stretching of the lattice distance of a PS colloidal crystal embedded in a PDMS elastomer matrix. b) Relationship between the reflectance peak positions and elongation of the silicone rubber sheet by stretching. The peak position shifted from 590 to 560 nm, and the reflectance intensity decreased gradually as indicated by the arrow. From Ref. [41]. 18
Figure 2. 9. Forces on superparamagnetic particles within a colloidal crystal array in the absence and presence of a magnetic field. Fer electrostatic repulsive force, F_{ma} magnetic dipole–magnetic dipole repulsive force, F_{m} external magnetic force, F_{mr} magnetic dipole–magnetic dipole attractive force. From Ref. [44]. 20
Figure 2. 10. Top: photographs of change in color of colloidal magnetite nanocrystals with increasing external magnetic field (from right to left). Bottom: dependence of the reflection spectrum on the sample with increasing magnetic field [7].. 21
Figure 2. 11. Excitation/detection instrumentation methods for PhC biosensors in label-free detection. A light bulb illuminates the crystal surface at normal incidence

through a fiber probe, and the reflected spectrum is gathered by a second fiber, connected to a spectrometer. 22
Figure 2. 12. Scheme and corresponding diffraction spectra of a colloidal PhC in the absence (top) and presence (bottom) of analyte. From Ref 50. 23
Figure 2. 13. Pictorial representation of use of glucose-sensing material to determine glucose concentration in tear fluid. From Ref 51. 23
Figure 2. 14. Schematic drawing of the guiding of light through an optical multi-mode step index fiber. 25
Figure 2. 15. Reflection spectra of PBG structure on the fiber optic tip exposed to different refractive index materials. From Ref. [65].. 27

Figure 3. 1. Scheme of dip coating assembly. 33
Figure 3. 2. SEM images of UV-Vis fiber optic tip with the assembled PS nanoparticles.. 33
Figure 3. 3. Comparison between the experimental and numerical reflection spectra of bare fiber and PhC assembly. 34
Figure 3. 4. HCP (left) and FCC (right) layer stacking sequences. 36
Figure 3. 5. (a) Unit cells from COMSOL simulations; (b) Reflectance spectra in HCP and FCC structures. 37
Figure 3. 6. Schematic illustration of the simulated PhC structure. a) top and (b) cross view of the simplified slab approach with the elementary cell highlighted in red; (c) hexagonal unit cell. 38
Figure 3. 7. Reflection spectra for different layers' number in air (a); simulated reflectance at peak wavelength vs number of layers (b); electrical field distribution at resonance wavelength (479 nm) (c) and away from resonance wavelength (345 nm) for the 7 layer structure (d). 40
Figure 3. 8. (a) Schematic view of the maximum incident angle; (b) unit cell with incident angle.. 42
Figure 3. 9. Spectra for different electromagnetic field incidence angles 43
Figure 3. 10. (a) Numerical reflection spectra for different nanospheres diameters; (b) bandgap wavelength vs nanospheres diameter. 44
Figure 3. 11. (a) Numerical reflection spectra for different nanospheres refractive indices in air; (b) Bandgap wavelength peak vs nanospheres refractive index. 45
Figure 3. 12. (a) Numerical reflection spectra for different external refractive index values; (b) bandgap wavelength vs external refractive index. 45
Figure 3. 13. (a) Experimental spectra for different surrounding refractive index; (b) experimental and numerical data vs different surrounding index. 47
Figure 3. 14. Schematic illustration of the period structure change of the PhC hydrogel in two different humidities conditions.. 50
Figure 3. 15. Digital photos of the as-prepared fiber optic sensors. Cross (a-b-c) and lateral (d-e-f) section of (a) bare fiber (b) PS nanoparticles and (c) PS nanoparticles infiltrated with acrylamide solution on the fiber tip. 52

List of Figures

Figure 3. 16. SEM images of the PhC on the tip of the fiber. (a) PS PhC (b) PS PhC hydrogel. 52
Figure 3. 17. Schematic illustration of reflection spectra experimental set up for the optical fiber tip humidity sensor. 54
Figure 3. 18. Reflectance spectra of optical fiber sensor under low (30% RH) (dark line) and high (90% RH) (red line) humidity conditions 55
Figure 3. 19. Peak position shift with time under different humidity conditions. At t=50 minutes the fiber optic sensor is in a closed chamber at RH 90%, the fiber is removed at 200 minutes and the sample returns to room conditions 56
Figure 3. 20. The reversible change in the diffraction wavelength of the photonic humidity sensor in 5 continuous cycles as the humidity switches between 10% and 100%. 57

Figure 4. 1. Scheme of dip coating assembly. 61
Figure 4. 2.SEM micrographs of a UV-VIS multimodal optical fiber tip surface after the nanobeads adsorption are shown at different level of magnification. The bar set at 2 μm allows to clearly see the periodic structure formed by the self-assembly of the beads on optical fiber tip. 61
Figure 4. 3. Reflectance spectra of PS beads self-assembled on the tip carried out in air (magenta solid line), water (blue line) and PBS 20 μM (light-blue line). 62
Figure 4. 4. Reflectance versus wavelength spectra after PS deposition exposed to PBS 20 μM, pH 7 (black line), in PBS after streptavidin (red line) solutions and in PBS after BSA exposure (blue line). 66
Figure 4. 5. Sensor wavelength vs. bBSA concentration for SA-bBSA system (dots) compared to the negative control BSA-bBSA system (cross) 67

Figure 5. 1. Scheme of preparation procedure of polymer coated magnetite particles. In the first step, dried hydrophobized magnetite nanoparticles are produced and in the second step transferred into an aqueous solution to form a ferrofluid. In the third step a styrene minimeulsion was obtained and then co-emulsified with the water-based ferrofluid from third step (fourth step). 76
Figure 5. 2. Schematic drawing of the microprocess 77
Figure 5. 3. Schematic view of the chemical preparation for the microprocess. 78
Figure 5. 4. Thermogravimetric curves of magnetite nanoparticles Mag 1 (solid line), Mag 10 (dash line) 80
Figure 5. 5. Thermogravimetric curves of samples. Latex 3 (black line), latex 5 (red line) and latex 7 (green line) 81
Figure 5. 6. TEM micrographs of Mag 10 (a) and Mag 1 (b) 82
Figure 5. 7. TEM micrograph of water-based ferrofluid (2nd step). 82
Figure 5. 8. TEM micrographs of Latex 1 (a) and Latex 2 (b-c) at different magnifications. 83

List of Figures

Figure 5. 9. TEM micrographs of Latex 3 at different magnifications.................. 84
Figure 5. 10. TEM micrographs of Latex 4 at different magnifications................ 85
Figure 5. 11. TEM micrographs of Latex 5 obtained by the one step batch miniemulsion method. 86
Figure 5. 12. Transmission electron micro TEM micrographs graph of Latex 6 (a-b) at different magnifications... 87
Figure 5. 13. Latex 7 micrographs at different magnifications. 87
Figure 5. 14. Thermogravimetric curve of Latex 7. 88
Figure 5. 15. Magnetization curves of magnetite/polystyrene nanoparticles at room temperature. 89

List of Tables

Table 5. 1. Preparation conditions. 75
Table 5. 2. Characteristics of the samples consisting of magnetite/polymer particles.. 79
Table 5. 3. Elemental composition of prepared samples. 88

Abbreviations

AA	Acrylic Acid
AAm	Acrylamide
bBSA	biotinylated Bovine Serum Albumin
BSA	Bovine Serum Albumin
BIS	N’-methylenebis(acrylamide)
CC	Colloidal Crystal
CMC	Critical Micelle Concentration
EDX	Energy Dispersive X-ray Analysis
FEM	Finite Element Method
FCC	Faced-Centered Cubic
FOS	Fiber Optic Sensor
HCP	Hexagonal Close Packed
HD	Hexadecane
HF	Hydrofluoric acid
ID	Inner Diameter
KPS	Potassium Peroxdisulfate
LCST	Low Critical Solution Temperature
LOD	Limit of Detection
LSPR	Localized Surface Plasmon Resonance
MMA	Methyl methacrylate
MMF	Multi-Mode Fibers
NA	Numerical Aperture
OD	Outer Diameter
PBG	Photonic BandGap
PBS	Phosphate Buffer Saline
PhCs	Photonic Crystals

Abbreviations

PAA	Polyacrilic Acid
PDMS	Poly(dimethylsiloxane)
PMMA	Polymethylmethacrylate
PML	Perfectly Matched Layer
PNIPAM	poly(N-isopropylacrylamide)
PS	Polystyrene
P(St-MMA-AA)	Poly(styrene-methyl methacrylate-acrylic acid)
RH	Relative Humidity
RI	Refractive Index
RIU	Refractive Index Unit
RPC	Responsive Photonic Crystal
SA	Streptavidin
SDS	Sodium Dodecyl Sulfate
SEM	Scanning Electron Microscopy
SERS	Surface Enhanced Raman Spectroscopy
SMF	Single-Mode Fibers
SRI	Surrounding Refractive Index
St	Styrene
TEM	Transmission Electron Microscopy
TGA	Thermogravimetic Analysis
VSM	Vibrating Sample Magnetometer

1.

Introduction

1.1. Motivation

Photonic crystals are structures with periodic dielectric modulation on the order of the wavelength of light; because of this periodicity, their study is analogous to the study of semiconductors in solid-state physics. The periodicity of the electronic potential in semiconductors, which is due to the regular arrangement of atoms in a lattice, gives rise to the electronic bandgaps, which are forbidden energy bands for electrons. Similarly, the periodicity of the refractive index (i.e., dielectric constant) gives rise to photonic bandgaps, forbidden energy bands for photons. Due to their artificial nature, the properties of photonic crystals can be tailored to satisfy specific needs.

When the refractive index of the dielectric material is sufficiently large, a complete photonic band gap is formed in which Bragg diffractions inhibit a range of wavelengths from propagating through the photonic crystal over all directions otherwise a photonic crystal made of dielectric materials with lower refractive indices have an incomplete band gap, and they can exhibit very unique optical properties. Natural examples of photonic crystals with incomplete bandgaps include opals that, despite being composed of the optically transparent silica, exhibit a bright display of colors. This variety of photonic crystal, with an incomplete photonic band gap, exhibits a stop bands which selected wavelengths of light are partially inhibited from propagating through the material in certain directions.

By organizing spherical colloids into a crystalline lattice, it is possible to obtain interesting functionality not only from the constituent material of the colloidal particles, but also, from the periodic structure associated with a crystalline lattice.

The wavelength of light diffracted from a colloidal crystal is directly proportional to several parameters, one of this is the lattice constant. Any variation in the lattice constant might lead to an observable shift in the stop band position. In this regard, colloidal crystals may represent a class of ideal candidates for fabricating optical sensors that can be used to monitor, measure and display environmental variations.

This work reports the fabrication and characterization of photonic bandgap crystal made of polymeric nanospheres that operates in the visible region of electromagnetic radiation. In particular, the photonic structures are realized on the tip of a multimode optical fiber in order to take advantages from fiber optic technology.

Fiber optic are compact and lightweight and minimally invasive materials and they should be immune to electromagnetic interference if no electrical currents flowing at the sensing point. Also, the fiber can be produced at relatively low or competitive cost.

The aim of this PhD thesis has been the development of composite polymeric nanoparticles and their application as optical sensors.

1.2. Thesis organization

The present dissertation is divided into four main parts, which reflect the tracks on which the research activity has been carried out. The Chapter 2 is dedicated to the literature background and comprises two different sections. The first section reviews the photonic crystal and responsive photonic crystals with examples application in different field, such as biosensors. The second section reviews the fiber optical tip sensors technology.

Chapter 3 presents a self-assembled colloidal photonic crystal on the fiber optic tip as a sensing probe. Results of optical measurements were compared to theoretical predictions. A strong agreement was found between the spectral positions of the optical reflections and those predicted by the Bragg diffraction model. Also, several numerical analyses were carried out to investigate different parameters such as the influence of the incident angle of the light, the external refractive index, the diameter of the nanospheres and the refractive index of the nanoparticles on the optical properties.

Chapter 4 shows the self-assembled colloidal photonic crystals on the fiber optic tip described in the Chapter 3 for the detection of biotinylated Bovine Serum Albumin. In this technology, the current detection limit of molecular recognition is overtaken up to femtomolar to demonstrate the high-performance level of photonic structures.

In the Chapter 5 a preliminary study for the encapsulation of magnetite nanoparticles in polymeric matrix is reported. The magnetic materials are promising as prospective components of photonic crystal because they allow to tune the optical properties under a magnetic field action.

The main characteristic of this class of photonic crystal is the presence of magnetically ordered components. Homogeneity and reproducibility of the composites polymer particles are fundamental requirements for their uniform performances in optical applications.

A key challenge in the synthesis of multicomponent nanoparticles is obtaining the particles with reproducibility and monodispersity in a minimum number of preparation steps and, also, with well-defined surface and physiochemical properties. To progress in such criteria, the presented work demonstrates the possibility to use microfluidic apparatus compared to emulsion polymerization technique to obtain composite nanoparticles for sensor applications.

Finally, Chapter 6 concludes about the work accomplished during this PhD and gives some perspectives for future work.

2.

Background Literature

2.1 Photonic Crystal

Photonic crystals (PhCs) are a new class of optical system represented by natural or artificial structures with periodic modulation of the refractive index that can control the flow of light.

These materials present a periodicity in dielectric constant ε in one or more dimensions. Such periodicity, introduced at the optical wavelength scale, allow to control of the light propagation in such a structure along chosen direction. In analogy to band gaps for electrons in semiconductor, the PhC prohibits the propagation of photons with certain energies. These forbidden photon energies, or the corresponding wavelength range, represent a photonic band gap (PhBG)[1]. This physical phenomenon is based on constructively and destructively interfering diffraction of electromagnetic waves. At each interface where the refractive index changes, light is reflected and transmitted. If all scattered waves interfere destructively, so we have a photonic band-gap.

Three kinds of structures of PhCs may be discerned as shown in Figure 2. 1. One, two or three dimensional (1D 2D or 3D) PhC, this is due to the variations in the refractive index that exists only in one, two or three dimensions. 3D structures are also known as opals. This term originates from a class of minerals that shows such a periodic 3D arrangement. Opals are among the most colorful of all gems, they exhibit a play of color which consists of iridescent color that changes with the angle at which they are viewed. The origin of iridescence come from an ordered microstructure of closely packed silica spheres, which causes light to diffract from the planes of the spheres. Since the size of the silica nanospheres is in the order of hundreds of nanometers, the wavelength of the diffracted light is also on the order of hundreds of nanometers. This range of wavelength falls within the visible region of light, and can be detected by eyes.

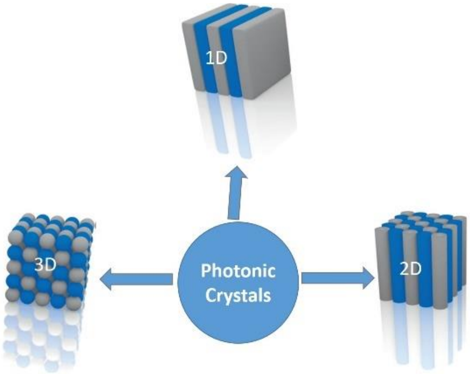

Figure 2. 1. Schematic illustration of 1D, 2D and 3D periodicity of photonic crystals structure. Adapted from Ref [3].

Studies on the fabrication of artificial PhC started intensively after the publication of two milestone papers in 1987 by *John and Yablonovitch* [1,2]. The fabrication methods can be classified into two groups: top-down and bottom-up approaches. The top-down approaches often use traditional microfabrication methods, such as photolithography and etching techniques, to produce microstructures with desired shape, size, and order from bulk materials. Bottom-up approaches generally involve the self-assembly of preformed building blocks into periodic photonic structures. The building blocks can be molecular species such as block copolymers or nanoscale objects such as SiO_2 or PS beads. Well-defined block copolymers can self-assemble into equilibrium phases consisting of one, two and three-dimensional periodic photonic structures, depending on the composition and architecture of block copolymer macromolecules [3,4]. In this case, the self-assembly process is a phase segregation process driven by the positive free energy of mixing of the chemically different polymer blocks. One challenge of the block copolymer photonic crystal systems is the small intrinsic dielectric contrast between typical copolymer microdomains, which makes it difficult to obtain large PBG in such materials.

Sub-micrometer colloidal spheres are the most favorable building blocks for the self-assembly of photonic crystals because they can be readily synthesized as monodisperse samples [5,6]. The properties of colloidal spheres can be further modified by coating them with a shell of a different chemical composition in varying thicknesses. When coating is performed uniformly, the resulting core–shell colloids can maintain their narrow size distribution. By controlling the structure, size, and composition of the shells, the optical, electrical, thermal, and catalytic properties of the spheres can be tuned over a broad range.

The assembly of colloids into 1D arrays can be easily prepared. *Ge et al.* reported the formation of 1D particle chains by self-assembly of superparamagnetic colloids using external magnetic fields [7,8].

The commonly used strategies to self-assemble monodispersed spherical colloids into ordered 2D arrays are based on the lateral capillary interaction, which originates from the deformation of the liquid surface [9,10]. The colloidal particles are typically assembled at the air–liquid interface or in a thin liquid layer supported on a flat solid substrate [11,12]. The arrays assembled on the surface of a liquid can be subsequently transferred onto various solid substrates if needed. When the assembly is performed on substrates, their surfaces must be flat, clean, and chemically homogeneous in order to generate a high-quality array with relatively large domain sizes of greater than hundreds of micrometers. Spin coating can be used to assist the assembly of colloids on a solid substrate [13]. An alternative method to create 2D arrays is electrophoretic deposition, which uses a strong electric field to assemble colloidal dispersions confined between two parallel solid electrodes [14–16].

With some modification, the methods used for 2D assembly can be employed to construct 3D crystals. To achieve a high degree of order and large domain sizes, several other methods have also been widely used for the assembly of 3D crystals, including those that use sedimentation, vertical deposition repulsive and physical confinement to assemble monodispersed colloids.

Sedimentation in a gravitational field seems to be the simplest approach for building 3D crystals [17]. While it can be carried out using simple setups, this method, in fact, involves several complex processes such as gravitational settling, Brownian motion, and crystallization (nucleation and growth). A number of parameters must be carefully chosen to grow highly ordered colloidal crystals with a large domain size, including the size, uniformity, and density of the colloids, as well as the rate of sedimentation. The main disadvantages of this method include a poor control over the morphology of the top surface, the thickness variations of the crystalline arrays, the long preparation time and the polycrystalline nature of the products.

The recently most widely used opal deposition method was introduced by *Jiang et al.* [18] and consists of immersing a substrate into a suspension vertically instead of horizontally. The authors coined the phrase “vertical deposition” for this method (Figure 2. 2). It uses the flow of suspension to the substrate induced by the evaporation of solvent in the already-deposited opal layer. This method turns out to have several advantages over sedimentation, such as a smaller amount of suspension needed, lower defect concentrations, easier sample handling, and good definition of the opal layer surface.

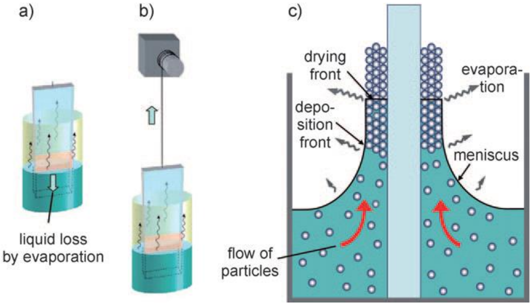

Figure 2. 2. Vertical deposition: a) Original setup; b) combination with slow lifting of the sample; c) assumed processes. (Picture parts are adapted from Ref. [20]) [6]

Vertical deposition is relatively slow as it relies on natural evaporation, and shows thickness gradients because the suspension concentration increases as the solvent evaporates [19] The growth can be efficiently influenced by many parameters, such as initial sphere volume fraction, temperature, relative humidity, substrate tilting angle and the substrate material [20,21].

It has been reported that monodispersed colloids also self-assemble into long-range-ordered lattices when they are subjected to a physical confinement provided, for example, by a pair of parallel substrates [22,23]. On the basis of this observation, *Xia et al.* demonstrated an effective approach that allowed for the fabrication of colloidal crystals with domain sizes as large as several square centimeters by using a specially designed packing cell [24–26]. A key to the success of this method is the continuous sonication, under which each particle in the colloid is placed at the lattice site that represents a thermodynamic minimum. This method is relatively fast, and it also provides tight control over the surface morphology and the number of layers of the crystalline assemblies.

Photonic materials with vivid structural colors exist commonly in Nature, and are found in species of birds, butterflies, insects, marine life and even flora [27,28]. Many organisms have the ability to tune their structural colors in response to surrounding environment for camouflage, warning about enemies or communication [27]. These organisms have the ability to control the transportation of light using periodical photonic nanostructure units located on the surface of their bodies [29].

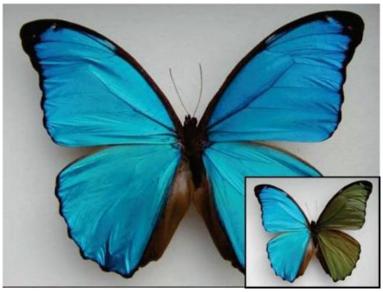

Among animals, butterflies (such as *Morpho Menelaus*) are the organism most commonly referred to illustrate this effect. The structural blue color originates from the diffraction of light and interference effects due to the presence of microstructures. (Figure 2. 3).

Figure 2. 3. Photograph of the wings of Morpho Menelaus butterfly. Inset, the right wing of the butterfly is wetted with ethanol. The change in the refractive index induces the color change from blue to green. From Ref [6].

Inspired by the tunable structural colors of these creatures, great effort has been devoted to exploring the mechanism and developing techniques to mimic the tunable colors of photonic materials. However, artificial photonic materials are much less smart than structures found in natural creatures.

From a physical point of view, PhC can be described as a periodic arrangement of regularly shaped materials whit different refractive index. A 3D PhC can be described by Bragg's law:

$$m\lambda = 2nd\ \sin\theta \quad \text{Equation 1}$$

where m is the order of diffraction, λ is the wavelength of incident light, n is the mean refractive index of the system composed of colloids and void, d is the spacing between the planes in lattice and θ is the angle between the incident light and diffraction crystal planes (Figure 2. 4).

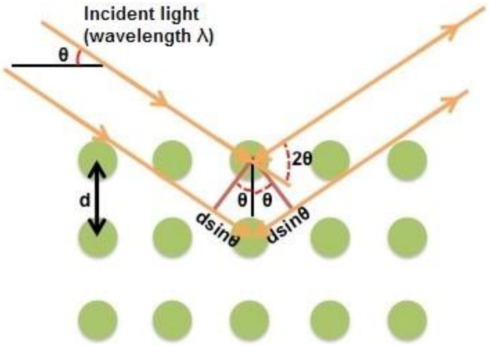

Figure 2. 4.Simplified scheme of light reflection from ordered spheres.

Under practical conditions, the colloidal spheres are embedded in matrix materials such as solvents and polymers, and combining Bragg's law with Snell's law of refraction leads to Equation 2, where d is the distance between particle planes, n_{eff} is the mean effective refractive index (RI), θ is the angle of incident light, m is the order of reflection, and λ is the wavelength of the reflected light. The reflected wavelength can also be calculated using the center-to-center distance D between the particles. The application of this method leads to Equation (3). The mean effective refractive index n_{eff} is defined as Equation (4), where n_p and n_m are the refractive indices of the particles and surrounding medium, respectively, and V_p and V_m are the respective volume fractions [30].

$$2d\left(n_{eff}^2 - sin^2\,\theta\right)^{1/2} = m\lambda \qquad \text{Equation 2}$$

$$\sqrt{\frac{8}{3}}\,D\left(n_{eff}^2 - sin^2\,\theta\right)^{1/2} = m\lambda \qquad \text{Equation 3}$$

$$n_{eff}^2 = n_p^2\,V_p + n_m^2\,V_m \qquad \text{Equation 4}$$

Based on Equation 2, there are several methods for tuning the structure, in principle, all the parameters that appears in equation 2 contributes to the determination of the diffraction wavelength and can be employed for the creation of RPCs. It is possible for example changing the interparticle distance D when the colloidal crystals are embedded in a polymer matrix that can expand or contract, such as hydrogel or elastic polymer. It is also possible to change the refractive index n_{eff} when you introduce in the system new substance, for example by selective or nonselective absorption or infiltration of solvents. Furthermore, the photonic properties can be tuned by changing the direction of the light θ.

Since the basic phenomenon of the band gap structure is diffraction, the periodicity of the refractive index has to have the same length-scale as half the wavelength. For a photonic crystal operating in the visible spectrum, it means that the period will be in the interval from 200 nm to 350 nm and the sizes of the colloids are typically in the range of 100 nm to 1 μm.

To use PhC as sensors, diffractions that fall into the visible range are usually preferred, as the optical output can be directly observed by the naked eye without the need of complicated and expensive apparatuses to read the signals. Moreover, considerations must be taken to ensure that the sensitivity, response rate, durability, and selectivity of the responsive system can meet the specific requirements of the sensor application. Generally, the photonic band gap can be reversibly changed in response to external physical or chemical stimuli.

2.2 Responsive Photonic Crystal

Responsive photonic crystals (RPC) are dielectrically periodical structures, that can alter their diffraction wavelength or intensities upon exposure to physical or chemical stimuli. In addition to the periodic structures that are required for traditional photonic crystals, a stimulus-responsive material has to be incorporated into the system. There are generally two approaches to introduce such responsive materials. In the first case, the responsive materials are directly prepared in the form of building blocks that can be used for constructing photonic crystals. A typical example is the 1D Bragg stacks formed by self-assembly of block copolymers that contain segments that can expand when exposed to certain solvents. In the second case, the periodic structures are defined first, and then the responsive materials are filled into the interstitial space to form a composite material that is optically tunable and mechanically stable. If the responsive material cannot provide enough mechanical strength, an inverse opal structure will be formed by first infiltrating an inert material into the interstitial space of the periodic structure to form a robust framework and then removing the original periodic template through calcination or chemical etching. Finally, the responsive materials are filled into the porous structure of the inverse opals.

In both cases, the responsive materials can be chosen from a wide variety of substances that can initiate changes in the lattice constant, refractive index, orientation, and order of the crystal structures. They typically include polymers, inorganic solids, and some molecular species. The general procedure in the design and fabrication of RPCs includes the selection of responsive materials according to specific needs, incorporation of the responsive materials into photonic crystals, and optimization of the performance of the photonic system. A good RPC is usually characterized by a high response rate, reversible tuning, a large tuning range of the diffraction wavelength or intensity, and the possibility to be miniaturized for integration into existing devices.

2.2.1 ThermoResponsive Photonic Crystals

Polymer-based thermosensitive photonic crystals were probably the first successful example of RPCs that combine a functional and responsive polymer matrix with colloidal crystals. Since the pioneering work by *Asher et al.* [31], a large number of RPCs have been developed that are similar in structure but sensitive to various stimuli. A classic system is composed of periodical materials that are created by embedding a non-close-packed colloidal crystal in a thermosensitive hydrogel of poly(N-isopropylacrylamide) (PNIPAM). PNIPAM is a thermosensitive polymer that undergoes a reversible volume phase transition between a hydrated state and a dehydrated state around its lower critical solution temperature (LCST, ca. 32 °C) in water. When the temperature increases, the polymer expels water and contracts so that the interparticle distance in the colloidal crystal decreases, leading to a blue shift in the diffraction. This hydrogel-colloidal crystal composite film shrinks and swells reversibly when the temperature is switched between 10 and 35°C. The diffraction wavelength can correspondingly be tuned between 704 and 460 nm, which covers the entire visible range.

*Takeoka and Watan*abe further extended the synthesis of thermoresponsive composite films, originally developed by *Asher et al.,* to the fabrication of a porous crystalline gel by templating against a close-packed silica colloidal crystal [32,33]. The porous gel was fabricated by polymerizing a solution mixture containing monomer, cross-linker, and initiator that was infiltrated into a preassembled silica colloidal crystal and then selectively removing the silica colloids by HF etching. Without the silica particles, the porous gel still showed a reversible photonic response to temperature change, thus suggesting that the voids left by the etching of silica still maintained a periodic arrangement (Figure 2. 5).

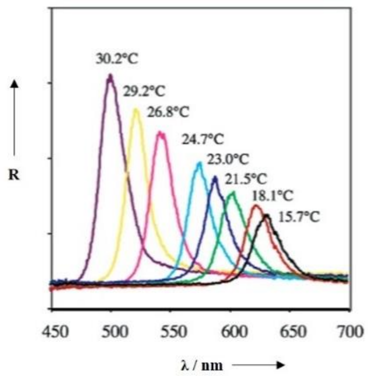

Figure 2. 5.Temperature dependence of the reflection spectrum of porous NIPAM gel built with a colloidal crystal template composed of silica nanoparticles (d=210 nm). From Ref. [33].

2.2.2 Chemically Responsive Photonic Crystals

Chemically RPCs are complex systems, as they cover the influence of various chemical species, including ions, solvent, vapor molecules and biomolecules, upon the optical properties of photonic crystals.

One may discern between chemically responsive PhCs based on porous structures with a tunable refractive index, and those based on the shrinking and swelling of polymers. The first are the materials of choice for distinguishing solvents through differences in the refractive index (RI). This RPC can distinguish many solvents, including methanol, ethanol, 2-propanol, tetrahydrofuran, dimethylformamide and toluene, as its diffraction red-shifted in high-RI solvents. This effect can be well explained by Bragg's law and Snell's law.

An example of this type of RPC are mesoporous (1D) Bragg stacks consisting of various inorganic materials that can differentiate organic solvents particularly well. The degree of compound uptake has to be closely controlled to achieve chemical selectivity when sensing changes in the refractive index. The small pore sizes in mesoporous materials allow for selective surface adsorption to have a significant impact on the total uptake of material as shown in the study of *Miguez et al.* [34]. They have realized an eight-layer Bragg stack made of SiO_2 and TiO_2 nanoparticles deposited alternately on the substrate by spin-coating, the specific color changes induced by the infiltration of solvents of different refractive indices makes these systems promising candidates to distinguish solvents such as water, ethylene glycol, and chlorobenzene (Figure 2. 6).

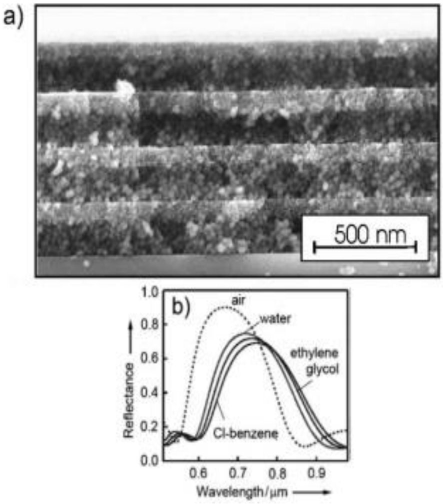

Figure 2. 6. a) SEM image of the cross section of an eight-layer Bragg reflector made of silica and titania nanoparticles deposited alternately on the substarte. b) Reflection of the Bragg reflector infiltrated with water, ethylene glycol and chlorobenzene. From Ref. [35].

The second type of chemically responsive PhCs is based on 3D swelling and shrinking of polymers. A useful development of such RPC is based on the changes in the lattice spacing determined by the filling ratio of the gaseous species for example for the humidity sensor [35–39].

Hydrogel-based sensors generally induce a diffraction wavelength shift in response to humidity changes, owing to the volume change of polymer networks. *Wang et al.* developed a humidity sensor by infiltrating acrylamide (AAm) solution into a P(St–MMA–AA) photonic crystal template and subsequently photo-polymerizing [36]. The colors of such sensors could reversibly vary from transparent to violet, blue, cyan, green and red under various humidity conditions, covering the whole visible range (Figure 2. 7).Furthermore, the color response showed exceptional stability under cyclic humidity experiments.

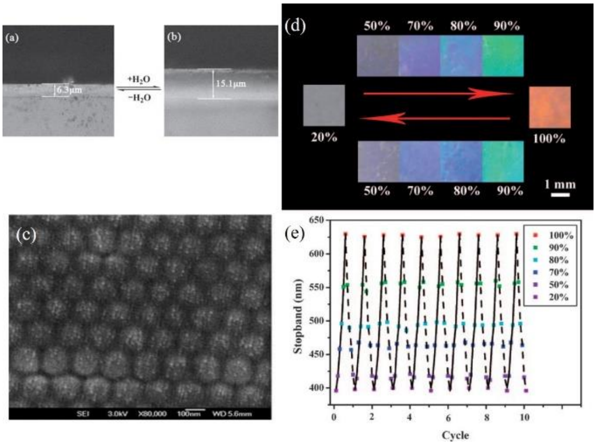

Figure 2. 7. (a) and (b) Typical microscope images of PAAm–P(St–MMA–AA) PC hydrogel (a) dry state, (b) wet state. (c) top view of the SEM image of PAAm–P(St–MMA–AA) PC hydrogel. (d) and (e) Reversible changes of the color/stopband of the PAAm–P(St–MMA–AA) PC hydrogel with relative humidity. (d) Photographs of the as-prepared PC hydrogel corresponding to different relative humidities (e) Reversible conversion of the stopband position of the PC hydrogel by alternately exposing to increasing and decreasing relative humidity conditions. From Ref. [37].

2.2.3 Mechanically Responsive Photonic Crystals

The mechanical RPCs are composite structures fabricated by infiltrating monomer or prepolymer into preassembled photonic crystal structures with subsequent thermo- or photopolymerization. The maximum ratio of mechanical pressing or stretching is determined by the elastic properties of the polymer matrix. While stretching is possible for most elastic systems, mechanical RPCs that can change color by pressing are usually fabricated from crystal templates with non-close packed structures. For composites composed of hydrogel and colloid crystals, the interparticle spacing can be 2.6 times greater than the particle size, which provides sufficient volume for compression of the lattice.

Fudouzi and Sawada have fabricated an elastic silicone sheet with reversibly tunable color by embedding a thin layer of PS colloidal crystals in poly(dimethylsiloxane) (PDMS) [40]. As schematically shown in Figure 2. 8, when this sheet was stretched in the horizontal direction, it was reduced in size in the vertical direction, thus leading to the decrease in the lattice distance and consequently to the blue shift of the diffraction peak. Figure 2.8 b shows that during stretching, the peak position shifted from 590 to 560 nm, and the reflectance intensity decreased gradually as indicated by the arrow. It has also been pointed out that when the stretching ratio is above a given value, the diffraction peak cannot be changed any further, as the colloidal particles come into contact with each other.

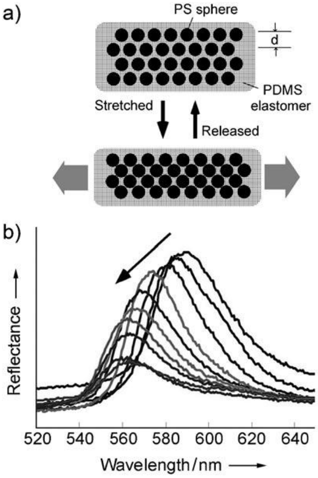

Figure 2. 8. a) Reversible tuning by stretching of the lattice distance of a PS colloidal crystal embedded in a PDMS elastomer matrix. b) Relationship between the reflectance peak positions and elongation of the silicone rubber sheet by stretching. The peak position shifted from 590 to 560 nm, and the reflectance intensity decreased gradually as indicated by the arrow. From Ref. [41].

2.2.4 Magnetically Responsive Photonic Crystals

Magnetic RPCs are a special case when compared with all the other RPCs prepared by coupling ordered structures with the responsive materials. In such systems, magnetic components are usually directly incorporated into colloidal building blocks that can respond to external fields without any additional special treatment

[7,41,42]. As the responsive mechanism is integrated into the building blocks, the performance of magnetic RPCs, such as the tuning range, response time, and so forth, is closely related to the properties of the specific magnetic colloids. The following requirements have to be considered in constructing a magnetic RPC: 1) The colloids are expected to possess a uniform shape, a controllable size, and a narrow size distribution so that the lattice constant can be precisely tuned and crystal defects can be eliminated as much as possible. 2) Materials with high refractive-index contrast to the surrounding medium are needed to obtain strong diffraction intensity. 3) Superparamagnetism of the colloids is essential for achieving reversible optical response, because significant magnetic interactions need to be initiated only through the application of external magnetic fields. 4) Colloidal particles made of pure magnetic materials with a high saturated magnetic moment are preferred, as they will favor a faster response to the external magnetic field and a lower responsive field strength threshold. 5) These magnetic particles are also expected to have appropriate surface properties that not only render the particles highly soluble in the dispersion medium but also produce sufficient repulsion to balance the magnetically induced attraction during the self-assembly process.

The application of a magnetic field to a solution containing magnetic colloids induces a magnetic packing force $F_m=\nabla(\mu B)$ that drags the particles toward the maximum of the local magnetic gradient, a magnetic attractive force $F_{ma}=6(\mu^2/d^4)$ between two adjacent particles lined up along the magnetic field, and a repulsive force $F_{mr}=3(\mu^2/d^4)$ between two particles that are arranged perpendicular to the field, where μ is the induced magnetic moment, B is the strength of the external field, and d is the interparticle spacing [43]. The highly charged surface of colloidal particles usually generates an electrostatic repulsive interaction $F_{er}=\pi\varepsilon\zeta^2\,\kappa\, r\, e^{-\kappa h}$, where ε is the dielectric constant, ζ is the zeta potential, κ^{-1} is the Debye–Hückel length, r is the particle radius, and h is the interparticle surface-to-surface distance (Figure 2. 9).

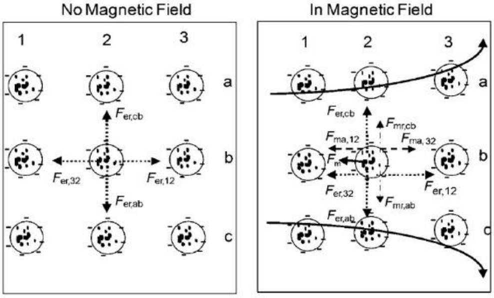

Figure 2. 9. Forces on superparamagnetic particles within a colloidal crystal array in the absence and presence of a magnetic field. Fer electrostatic repulsive force, F_{ma} magnetic dipole–magnetic dipole repulsive force, F_m external magnetic force, F_{mr} magnetic dipole–magnetic dipole attractive force. From Ref. [44].

If these forces are comparable in strength, any change to the force balance would alter the interparticle separation and assembly structure.

The key to the successful assembly of magnetic RPCs in aqueous solutions is the establishment of a balance between the field-induced magnetic attraction and the electrostatic repulsion.

Ge at al. have synthesized a nanocrystal colloidal clusters of magnetite (Fe_3O_4) with controllable uniform sizes in the range of approximately 30 to 200 nm [44]. Each Fe_3O_4 cluster is composed of many interconnected primary nanocrystals of approximately 10 nm diameter so that the clusters retain their superparamagnetic behavior at room temperature even though its overall size exceeds the critical size distinguishing ferromagnetic and superparamagnetic magnetite (30 nm). Thanks to a layer of covalently bonded polyelectrolyte surfactants, the Fe_3O_4 clusters possess a highly charged surface and disperse well in aqueous solution. This structure can readily assemble in almost any kind of solvent into photonic structures that display brilliant colors from red to blue when the strength of the applied magnetic field is increased [7,45,46]. Figure 2. 10 shows photographs of colloidal photonic crystals self-assembled in water in response to a varying external magnetic field as well as the reflection spectra displaying the dependence of the diffraction peak on the sample–magnet distance. Such optical response to the external magnetic field is instant and fully reversible, and may cover a wide spectrum range.

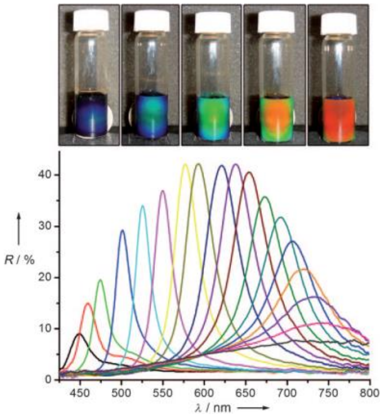

Figure 2. 10. Top: photographs of change in color of colloidal magnetite nanocrystals with increasing external magnetic field (from right to left). Bottom: dependence of the reflection spectrum on the sample with increasing magnetic field [7].

To achieve periodic arrangement in solvents other than water, the nanocrystals are typically covered with a silica shell to form more stable dispersions [47].

To tune the diffraction wavelength, one important parameter is the particle size [8]. Generally, smaller colloidal magnetite nanocrystals (under 100 nm) form ordered structures only under strong magnetic fields and preferably diffract blue light. Larger clusters (over 150 nm) diffract red light in a relatively weak magnetic field, and the ordered structure may become unstable if the external field becomes too strong. Medium size clusters (ca. 100–150 nm) self-assemble into stable ordered structures with tunable diffraction covering the entire visible spectrum.

2.3 Biosensor based on Photonic Crystals

Biosensors make use of biological components such as enzymes, antibodies, aptamers, and gene probes to recognize a specific target [48]. Typical applications of such sensors are in the screening of compound libraries and of ligand–receptor interactions (such as between biotin and streptavidin), in label-free optical detection, and in studies on cell morphology. The interactions of analyte and probe molecules on the PhC will result in some physicochemical changes of the films, such as refractive index, diffracting plane spacing or both of them. These changes of the PhC structure could be detected as the shift of their Bragg diffraction peaks.
Because only the Bragg diffraction peak of the PhC need to be observed during all the procedure of bioassay, the devices are extremely simple. As shown in Figure 2. 11, only one white light source, one spectrometer, and optical fibers are needed in the biosensor device.

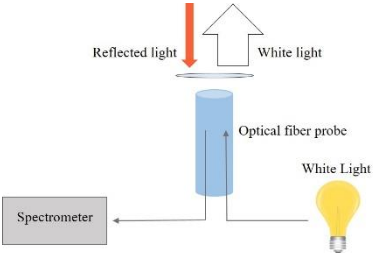

Figure 2. 11. Excitation/detection instrumentation methods for PhC biosensors in label-free detection. A light bulb illuminates the crystal surface at normal incidence through a fiber probe, and the reflected spectrum is gathered by a second fiber, connected to a spectrometer.

Asher and co-workers have developed a colloidal crystal film biosensor for glucose detection[49]. They designed a crystalline colloidal array of monodispersed nanoparticles embedded within a glucose-responsive hydrogel matrix. The resulting material swelled reversibly in the presence of glucose. The swelling event increases the mean separation between the immobilized colloidal nanoparticles, shifting the Bragg peak of diffracted light to longer wavelengths and producing a red-shift in the optical properties of the colloidal PhC (Figure 2. 12).

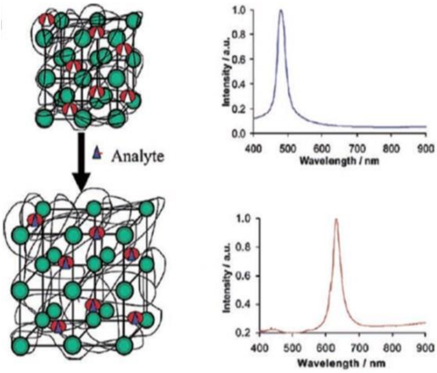

Figure 2. 12. Scheme and corresponding diffraction spectra of a colloidal PhC in the absence (top) and presence (bottom) of analyte. From Ref [50].

This sensing motif could be utilized for the fabrication of noninvasive or minimally invasive in vivo glucose sensing materials in the form of ocular inserts or diagnostic contact lenses for patients with diabetes mellitus (Figure 2. 13) [50].

Figure 2. 13. Pictorial representation of use of glucose-sensing material to determine glucose concentration in tear fluid. From Ref [51].

Alieva et al. have modified a silicate layer that forms the top of an SiO_2/Ta_2O_5 Bragg stack with streptavidin (each molecule of which can bind four biotin molecules) [51]. On binding biotin, the refractive index of the top layer changes, and this results in a wavelength shift of the reflected light. Biotin can be monitored by this method with a limit of detection (LOD) of 3 μg mL^{-1}.

2.4 The Optical Fiber Tip Sensors

Optical fibers are flexible, transparent fibers made by drawing glass or plastic to a small diameter. They usually consist of a core with refractive index n_1, surrounded by a cladding with a lower refractive index n_2. The fiber acts as a waveguide due to total internal reflection. The light propagation inside the core will be totally reflected at the interface between the core and the cladding layer when the incident angle is larger than the critical angle θ_c and will be well confined in the core. According to Snell's law, the critical angle is determined by the refractive index of the core and cladding:

$$\theta_c = \sin^{-1}\frac{n_2}{n_1} \qquad \text{Equation 5}$$

The optical ray with the maximum incident angle θ_1 near $\pi/2$ is called the fundamental mode, whereas rays with smaller angle θ_2, but still larger than θ_c can also propagate in the fiber and are called high order modes. When the core radius is small enough and/or the index step is low enough, only the fundamental mode can propagate inside. Such fibers are called single-mode fibers (SMF); the other type of fibers being a multi-mode fibers (MMF). The mode characteristics depend also on wavelength. A fiber can be SMF for longer wavelengths, but becomes an MMF for shorter wavelengths [52].

If a ray enters the optical fiber (Figure 2. 14) with an angel below the acceptance angle θ_a, it will arrive at the core-cladding interface at an angle $\theta_1 > \theta_c$ and it will be totally reflected and can be transmitted with relative little loss in energy over long distances. In contrast, light that enters the optical fiber at an angle larger than θ_a will hit the core-cladding interface at an angle $\theta_2 < \theta_c$ and will not be totally reflected. At each reflection, some of the light will dissipate in the cladding until total dissipation by absorption in the cladding and scattering out of the cladding.

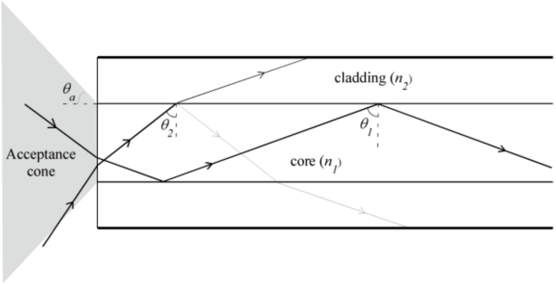

Figure 2. 14. Schematic drawing of the guiding of light through an optical multi-mode step index fiber.

The range of angles over which wave guiding occurs within an optical fiber defines the numerical aperture (NA) of the fiber and can be calculated from the refractive indices of the core (n_1), the cladding (n_2), and the surrounding media (n_0).

$$NA = n_0 \sin\theta_a = n_0\sqrt{n_1^2 - n_2^2} \quad \text{Equation 6}$$

In air $n_0 = 1$ and in water $n_0 \approx 1.33$ [53].

The possibility to produce fiber optic sensor (FOS) comes from the sensitive of the fiber to any parameter which can modify the intensity, frequency, polarization, or phase of light travelling through the fiber. Also, optical fiber has certain advantages such as immunity to electromagnetic interference, lightweight, small size and high sensitivity.

FOSs may be categorized according to various classification schemes. Based on one scheme, they are classified as intrinsic if the effect of the measurand on the light being transmitted takes place in the fiber. The sensor is considered to be extrinsic if the fiber carries the light from the source and to the detector, but the modulation occurs outside the fiber. In this case, the optical fiber is simply used to guide the light to and from a location at which an optical sensor head is located. The sensor head is external to the optical fiber and is usually based on miniature optical components, which are designed to modulate the properties of light in response to changes in the environment with respect to physical perturbations of interest. Thus, in this configuration, one fiber transmits optical energy to the sensor head. Then this light is appropriately modulated and is coupled back via a second fiber, which guides it to the optical detector. Extrinsic fiber optic sensors use a fiber optic cable, normally a multimode one, to transmit modulated light from a conventional sensor. A major feature of extrinsic sensors, which makes them so useful in such a large number of applications, is their ability to reach places which are otherwise inaccessible.

Among all the possibility to develop a FOS, we are interest to use the tip of an optical fiber for the development of new platform sensor for micro and nanotechnologies.

The flat tip of an optical fiber is a uniquely unconventional substrate. Its microscopic cross section and large aspect ratio provide access to remote and confined environments, while its biocompatibility, all-optical interrogation, and mechanical robustness provide access to hostile environments that feature extremes of temperature, pressure and electromagnetic interference.

More recently, the field of ‘lab on a fiber’ has emerged, giving rise to state-of-the-art fiber sensing applications that rely on micro- and nano fabrication of devices at the end of the fiber [54–56].

Many dedicated technological approaches have been developed to manufacture resonant structures on standard or specially designed fiber tips [57–59]. In most cases, the resonant structures are combined with plasmonic effects in order to enhance the sensing features of the final devices [60–63]. On this argument, the most promising configuration seems based on hybrid metallo-dielectric nanostructure supporting localized surface plasmon resonance (LSPRs) and surface enhanced Raman scattering (SERS).

The simplest approach to functionalizing the tip of an optical fiber is the self-assembly. Under appropriate conditions, stochastic assemblies of monodisperse objects can be produced, where the most common strategies employ colloids, nanoparticles, thin film deposition techniques and even simple surface roughening.

While these techniques sacrifice the geometrical control offered by more precise lithographic techniques, they offer the benefit of low overhead cost, providing ready access to the nano-regime.

Furthermore, the challenge in exploiting the photonic bandgap sensing features in miniaturized optical fiber devices favorites the introduction of a large number of sensing configurations realized on the tip of the optical fiber.

Haibin at al. [64] realized a fiber capillary structure which helps the self-assembly of polystyrene nanoparticles on the fiber optic tip. They also used this structure to measure the reflection index difference of two different solvent to develop a gas sensor made of PhC (Figure 2. 15).

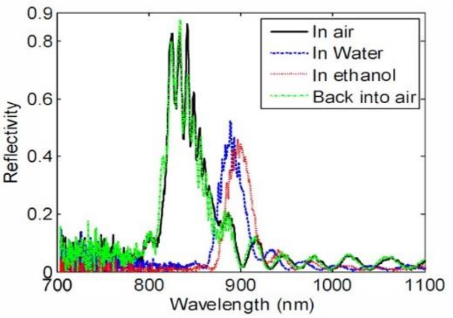

Figure 2. 15. Reflection spectra of PBG structure on the fiber optic tip exposed to different refractive index materials. From Ref. [65].

Cusano et al. [65] suggested a fabrication route for self-assembling periodic patterns on optical fiber tips. The technique was based on self-assembling polystyrene microspheres at the air/water interface and on successive transferring of the monolayer colloidal crystal on the fiber tip. By applying to the fiber further treatments like particle size reduction, metal coating and sphere removal, different periodic structures were realized. The results obtained indicate that self- assembly technique affords opportunity to create on the optical fiber tip dielectric and metallic dielectric spheres' arrays with a feature size down to a submicron scale or metallic patterns with a few hundred nanometers at low fabrication costs.

FOS are powerful detection tools that have wide applications in biomedical research also. Optical biosensing is often based on the detection of a fluorescence signal, that generally require the use of a fluorescence moiety. These methods are addressed as label-needing assays as either the target molecules (the biomarker to be detected) or the bio-recognition element (the capturing molecule that selectively interacts with the biomarker) are labeled with a fluorescent tag, such as dyes. The modulation of the optical properties of the tag, generally the intensity of the fluorescence under UV illumination, indicates the formation of a complex between the capturing and the target molecules and the strength of the interaction as well. The fluorescence-based detection is extremely sensitive being able to reliably detect down to the pico molar limit (10^{-12} M, pM) [66], its reliable and high-throughput. However, it suffers from the need to put in place laborious labeling processes that may also interfere with the function of a biomolecule. Moreover ultra-low-concentration quantitative analysis can be challenging due to the so called fluorescence signal bias, as the number of fluorophores on each molecule cannot be precisely controlled [67,68].

In contrast, in label-free assays, the target or the capturing molecules are not labeled or altered in any way, and their interaction is detected directly with other molecular system interfering with the complex formation. This type of detection is relatively easy and cheaper to perform, and allows for quantitative and kinetic measurement of molecular interaction. A fast growing label-free bio-detection approach measures the refractive index (RI) change induced by the selective interaction between biomolecular systems, which is related to the sample concentration or its surface density. This characteristic is particularly attractive when ultrasmall (femtoliter to nanoliter) detection volumes are available. Despite the elicited differences, both fluorescence-based and label-free detection, are being widely used in optical sensors and provide complementary information regarding interactions among biomolecules, which makes optical sensors more versatile than other types of sensing technologies, such as surface acoustic wave and quartz crystal microbalance where only label-free detection can be implemented [69]. Among the biosensors based on RI detection, recently, a wide range of PhC based sensing devices have been proposed and investigated. They have been proven to be suitable in general-purpose disposable biosensor platform to perform a variety of biochemical and cellular assays.

Biosensors based on PhCs, have been widely used to detect refractive index (RI) changes induced by surface-attached biomaterials as well as analytes that attach to surface confined capturing molecules, spanning a wide range of dimensions and biochemical functionalities [70–72].

In sensor development, sensitivity is a critically important parameter to assess the sensor performance level. The sensitivity is the slope of the linear branch of the sensor dose curve, namely the curve where the sensor's relative signal change is plotted *vs.* the analyte concentration. The larger the strength of light-matter interaction the more sensitive the sensor is [73–75]. In most evanescent wave based sensors, the output signal, and therefore the device sensitivity can be limited by the fraction of light dispersed in solution or at the sensor surface. The use of PhCs on the fiber tip offer a number of unique advantages in fact due to the presence of air holes running along its entire tip fiber length, these have a unique ability to accommodate biological and chemical samples in gaseous or liquid forms in the immediate vicinity of the fiber core. PhCs can be used simultaneously for light guiding and as a fluidic channel, leading to a strong light/sample overlap. Such beads can be further functionalized with biorecognition layers that can bind and progressively accumulate target biomolecules, thus enhancing sensor sensitivity and specificity. The sensor performance is also characterized by limit of detection (LOD). The LOD is, according to IUPAC (reference), the average of the blank signal plus three times the blank standard deviation. Brucka et al. [76] developed a Mach-Zehnder interferometer biosensor based on a high index contrast polymer material system and the demonstration of label-free online measurement of biotin–streptavidin binding on the sensor surface. They found a detection limit of 100 μM. Voisin et al. [77], studied and developed a SPR optical fiber biosensors constitute a miniaturized counterpart to the bulky prism configuration and offer remote operation in very small volumes of analyte; moreover they used the biotin–streptavidin complex as a benchmark, they reported a limit of detection as low as 2 pM. Among these approaches, PhC biosensors offer a rapid and sensitive optical detection method for biomolecules, cells and viruses by monitoring the refractive index variation.

3.

Self-assembled colloidal photonic crystal on the fiber optic tip and its application[1]

3.1 Abstract

In this chapter an effective and efficient method to fabricate fiber optic sensing probes based on the self -assembly of polymer nanoparticles is presented. A 3D photonic crystal (PhC), dielectric structure consisting of three-dimensional close-packed array of submicrometer spheres, has been deposited on the tip of an optical multimode fiber by a self-assembly technique. The spectral response in reflection is directly measured being the optical fiber itself the light coupling substrate. The reflected optical signal relies on the spectral features of the assembled colloidal crystal exhibiting a resonance band due to the bandgap of the photonic structure of the crystal.

Also, a numerical tool based on finite element method (FEM) analysis has been developed to study and to analyze the 3D subwavelength structures (This analysis

---

[1] *This chapter is partially adapted from the following article: P. Di Palma, C. Taddei, A: Borriello, G. De Luca; A. Iadicicco, M. Giordano; S. Campopiano, L. Sansone. Self-assembled colloidal photonic crystal on the fiber optic tip as a sensing probe. IEEE Photonics Journal (2017)*
DOI: 10.1109/JPHOT.2017.2689075

was conducted in collaboration with the Department of Engineering, University of Naples "Parthenope"). Numerical results are in good agreement with the observed experimental spectra. Moreover, refractive index measurements have been carried out revealing a sensitivity of up to 445 nm/RIU, in the refractive index range from 1.33 to 1.36. The achieved performances, obtained using very small active areas and very easy and reliable fabrication procedure, demonstrate the future perspectives of these fiber-optic probes for chemical and biological sensing applications. In the last part of this chapter, a humidity sensor application is reported.

3.2 Materials and Procedure

Materials.

Monodispersed polystyrene (PS) beads (aqueous dispersions, 10% w/w) were purchased from Sigma Aldrich (Italy) and used as received. The particles used in this study have a diameter of 200 nm (from data sheet).

Particle Deposition.

An UV-VIS multimode fiber optic, 200 µm core (Thorlabs, U.S.A.) was cut by using a high precision cleaver (Fujikura, Tokio), and successively dip-coated vertically from the colloidal PS suspension, performed by means of an automated system dip coater (NIMA Technology Micro-Processor Interface IU4, Spain) at an immersion/extraction speed of 107 mm/min (Figure 3. 1). After the evaporation of solvent, a PS pattern was formed on the tip of the optical fiber.

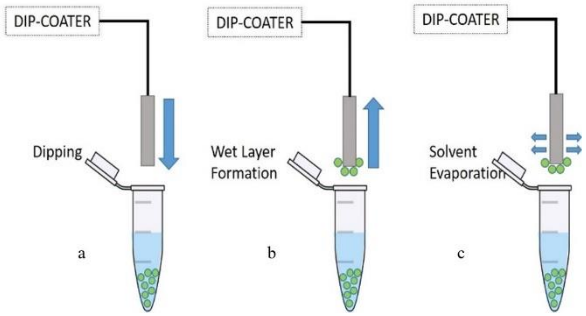

Figure 3. 1. Scheme of dip coating assembly.

Figure 3. 2 shows scanning electron microscopy (SEM) micrographs (for more details see Appendix I – Characterization Technique) at different degree of magnifications.

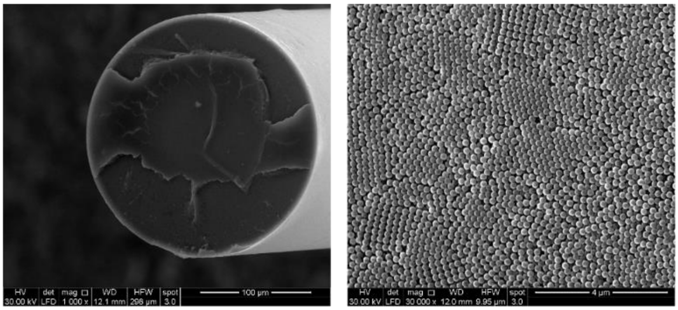

Figure 3. 2. SEM images of UV-Vis fiber optic tip with the assembled PS nanoparticles

3.3 Spectral Characterization

The PhC structures self-assembled on the fiber tip were also optically characterized in visible range. Reflectance measurements were carried out by illuminating the fiber tip with a xenon optical source and redirecting the reflected light to an optical spectrum analyzer by means of a 3dB directional coupler (for more details see Appendix I - Optoelectronic set up).

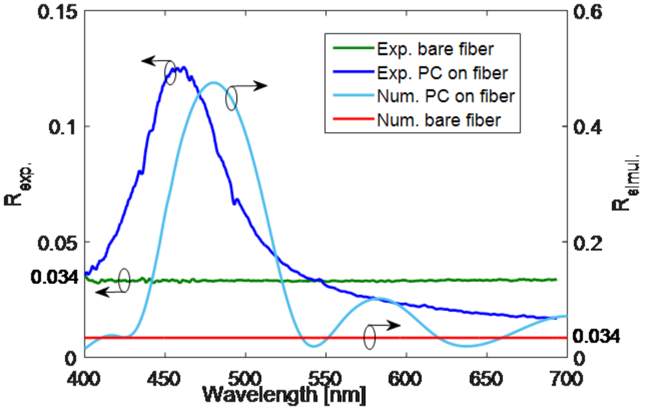

Figure 3. 3. Comparison between the experimental and numerical reflection spectra of bare fiber and PhC assembly.

Figure 3. 3 shows the experimental reflectance spectrum of PS assembly on the fiber tip in comparison with the reflectance spectrum of the bare fiber tip; moreover, the results of the numerical simulations are reported in the same figure. Reflectance spectra were normalized to the incident power and taking into consideration the lab-grade fiber splitters (see Appendix I – Optoelectronic set up). The bare fiber tip reflectance spectrum exhibits a quasi-constant value of about 3.4% in agreement with expected amount of light that is reflected back from the interface fiber glass – air. When the PS nanospheres are deposited on the fiber tip, the experimental spectrum shows a peak with a maximum of about 12.5% centered at 458 nm with a 3dB bandwidth of 54 nm. Therefore, in comparison with the bare fiber (our reference) it is obtained an enhancement of about 3.7. Out of the peak band, the reflectance of the PhC structure formed by the PS nanospheres is almost comparable with the bare fiber one confirming that the wavelength selective enhancement of the reflectance is due to a bandgap phenomenon of the self-assembled nanospheres.

The main appreciable difference is the peak amplitude values, 12,5% and 47% for the experimental and numerical data, respectively. Moreover, the numerical peak exhibits a red shift of 20 nm as compared with the experimental one. These mismatches can be explained considering the unavoidable fabrication defects with respect to the ideal structure considered in the numerical analysis as well as tolerances in the nanospheres diameter and refractive index.

3.4 Numerical Analysis

Method

The simulations were carried out via FEM using the commercial modeling tool COMSOL Multiphysics – RF Module (COMSOL Inc., Burlington, MA, USA). The computational domain is composed of an elementary cell of the periodic nanostructure containing: i) a layer of glass, ii) polystyrene beads, and iii) surrounding media. The simulation region has periodic Floquet boundary condition in three directions in plane xy staggered of 120° and Perfectly Matched Layer (PML) absorbing boundary condition in the z direction for consider an indefinite media above our structure, hence for doesn't considering the reflectivity contribution of the truncation domain. The excitation port was put on the final glass surface and the same port were used to collect reflection spectra also. Appropriated dispersion tables [78,79] were used for the refractive indexes.

The simulations were performed on the CRESCO Enea's mainframe with 12 core processors and 128 GB RAM.

Choice of the unit cell.

From the SEM images of the nanostructures (Figure 3. 2) it seems that in the nanosphere films we can observe the presence of a regularly packed array (triangular arrangement) corresponding either to the (111) surface of a faced-centered cubic (FCC) system and/or to the (001) surface of a hexagonal close packed (HCP) one (a schematic view of FCC and HCP layer stacking sequences is plotted in Figure 3. 4. It is reasonable to believe that in our film both FCC and HCP lattice packings coexist [80].

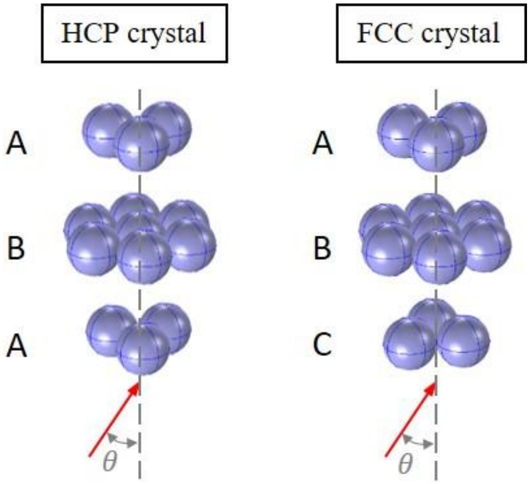

Figure 3. 4. HCP (left) and FCC (right) layer stacking sequences.

Furthermore, for the optical behavior of the proposed sensing probe, it is worth highlighting that the two photonic crystal structures, HCP and FCC, are equivalent in terms of resonance wavelength. Indeed, taking into consideration the Bragg's law for a PhC and an incident plane wave with angle θ, the resonance wavelength λ can be expressed as:

$$\lambda = 2n_{eff} d \cos\theta \qquad \text{Equation 7}$$

where the interplanar spacing d is the same for (111) FCC and (001) HCP crystals and is estimated from the relation $d = 0.816\,D$, with D equal to the effective particle diameter. Similarly, $n_{eff} = \phi n_p + (1 - \phi) n_m$, where the filling factor $\phi = 0.74$ is the same for both the arrangements.

In order to assess the similarity, we have calculated the reflected spectra of CC layers with both lattice packings by FEM analysis. Figure 3. 5 (a) shows the 3D unit cells used for the COMSOL simulations of the two different arrangements with seven layers of nanospheres. The simulated reflected spectra are plotted in Figure 3. 5 (b), where it is possible to observe a perfect overlap of the reflectance spectra in the FCC and HCP arrangements.

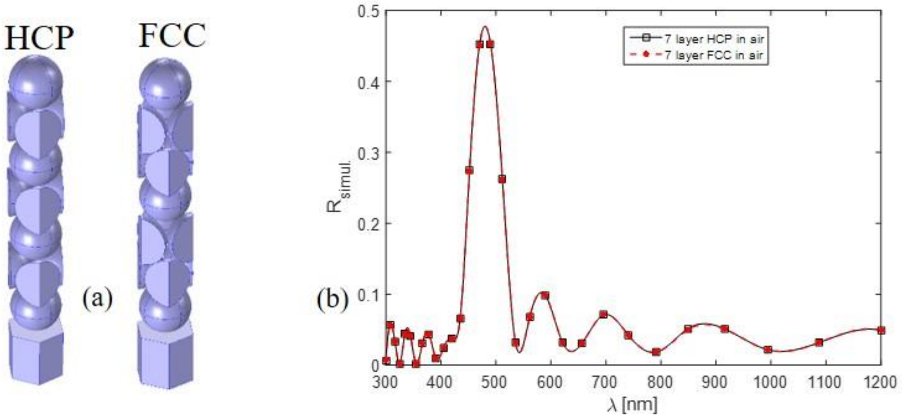

Figure 3. 5. (a) Unit cells from COMSOL simulations; (b) Reflectance spectra in HCP and FCC structures.

According to the previous considerations, in the following, the HCP structure with nanospheres diameter of 200 nm and refractive index of 1,59 are selected for the following analysis. To simplify the photonic crystals reflectance computation, the simulated structure does not take into account the finite size of the lattice (as the real one).

The 3D structure considered in this study is schematically represented in Figure 3. 6.

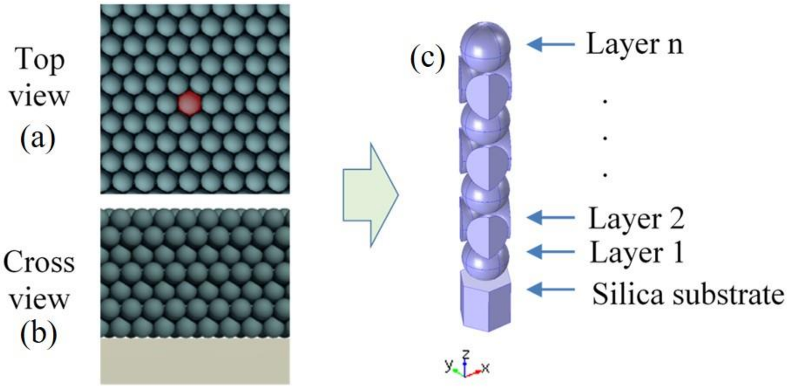

Figure 3. 6. Schematic illustration of the simulated PhC structure. a) top and (b) cross view of the simplified slab approach with the elementary cell highlighted in red; (c) hexagonal unit cell.

It principally consists of a silica glass substrate covered with a polystyrene nanospheres hexagonal close packed (HCP) lattice, hence with a filling factor $k_f = \frac{\pi}{3\sqrt{2}} = 0.7405$. Figure 3. 6 (a) and (b) show schematic top and cross view of the 3D colloidal crystal. When such structure is illuminated with a plane wave orthogonal to the silica surface, photonic resonances are expected to be excited due to the phase matching condition between the scattered waves and the modes supported by the crystal, depending on the geometric features of the structure itself.

A common approach requires the calculation of the scattering parameters of a slab that can be simulated as the unit cell with periodic boundary condition [81,82]. The unit cell consists in a hexagonal silica glass base that inscribes a circumference with radius like that of the nanospheres, as shown the Figure 3. 6 (c). The different layers of nanospheres alternatively consist in: (a) a single nanosphere and (b) in three wedges of nanosphere each of that like a third of nanospheres. This arrangement is due to their honeycomb organization that is the HCP lattice. The refractive indices used for modeling silica and polystyrene nanosphere of the unit cell in the investigated wavelength domain were taken from [78] and [79] respectively, whereas the nanospheres diameter was d = 200 nm according to the datasheet. Afterwards we will consider small variations of these values to study the effect on the reflected spectrum.

The Perfectly Matched Layer (PML) absorbing boundary condition in the z direction over the nanospheres multilayer were used to consider an indefinite surrounding media over the PhC structure. Periodic Floquet boundary condition in three directions in plane xy staggered of 120° placed two-by-two in the opposite walls were used to implement the periodicity.

It is worth noting that the number of layer plays an important role in the shape and amplitude of the resonance band in the reflected signal.

Figure 3. 7 shows the numerical reflectance spectra (normalized to the incident field power) for different numbers of layers. As evident, the reflectance spectra show a positive peak in the reflected signal (highlighting enhancement in the reflected power) that clearly depends on the number of layers: the resonant wavelength exhibits a blue shift with the number of layers whereas the peak amplitude strongly increases. Increasing the number of the layers, the reflected spectra clearly show a narrow band enhancement in reflected power due to photonic bandgap effect in CC structure. The Figure 3. 7 (b) summarizes the peak dependence on the number of layers up to 10 layers. The resonant wavelength exhibits a blue shift with a convergent trend versus the number of the layers. It becomes almost constant with number of layers higher than 7. A different behavior takes place about the peak amplitude: it constantly increases with the simulated number of layers up to 10. It is reasonable to believe that the maximum reflectance can reach the 100% with increasing number of layers. However, the layers’ number were limited to 10 for computational reason. In addition, the secondary lobes do not increase their amplitude, thus the ratio between main and secondary lobe rises by increasing the number of layers. From these results, in order to limit the computational efforts, in the following analysis the number of layers is fixed to 7.

Figure 3. 7 (c) and (d) show the electrical field distribution at resonance wavelength (479 nm) and away from resonance wavelength (345 nm), respectively, for the 7-layer structure. The figures plot the field distribution in two perpendicular plans cutting the unit cell in the center and on the nanosphere surface. In both graphs, a significant field localization can be clearly observed at the interfaces between the PS nanospheres and surrounding dielectric (air in our case). This can be attributed to localized reflection-refraction of the electrical field due to difference in the refractive index (PS – air).

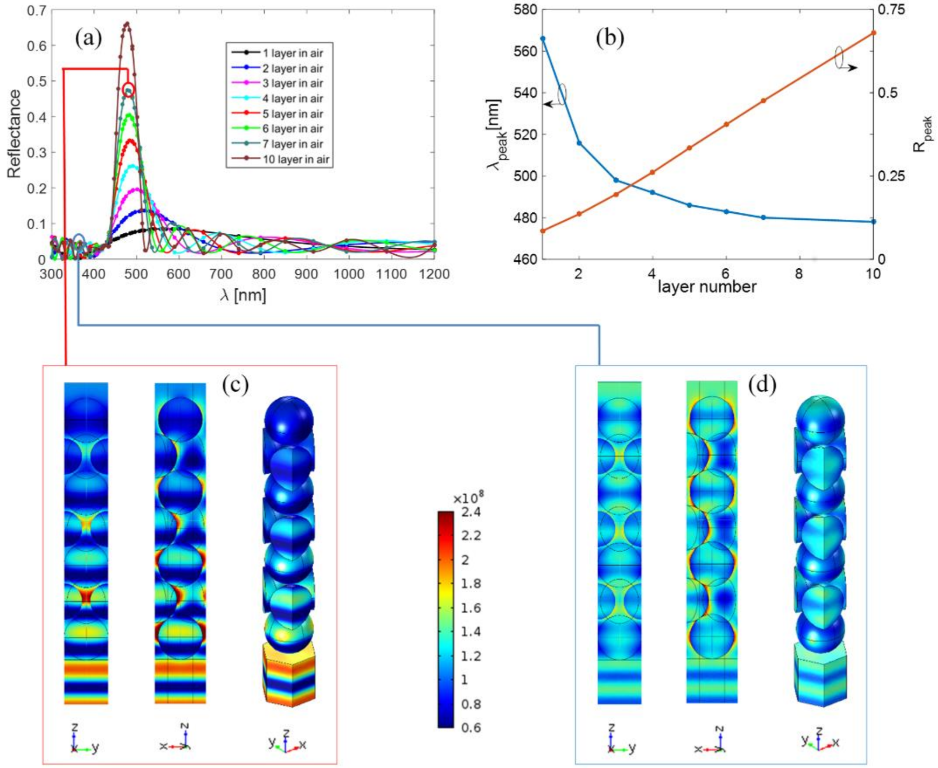

Figure 3. 7. Reflection spectra for different layers' number in air (a); simulated reflectance at peak wavelength vs number of layers (b); electrical field distribution at resonance wavelength (479 nm) (c) and away from resonance wavelength (345 nm) for the 7 layer structure (d).

A thorough numerical analysis was conducted to validate the experimental results and to investigate the dependence of the bandgap wavelength on the physical and geometrical features on the self-assembly. It is worth to highlight that the simulated planar structure slightly differs from the real device (PhC on fiber tip) principally for the endless edges and for the incident excitation that does not take into consideration a Gaussian-like distribution as result from high number of modes incident with several different angles at the interface silica-PhC. To assess this last approximation, we provide simulation with different angles of the incidence beam, ranging in the range of 0-9°, in accord with the fiber optic NA.

Dependence on incident angle.

This analysis is aimed to take into account the multimodal nature of the optical fiber, the Thorlabs 0.22 NA TECS, which supports high order modes. The numerical aperture of the selected fiber is equal to $NA = 0.22$. Consequently, the maximum angle formed by the incident beam with the glass surface normal θ_G (see Figure 3. 8 (a)) can be expressed as:

$$n_G \cdot \sin(\theta_{Gmax}) = n_0 \cdot \sin(\theta_0) = NA \qquad \text{Equation 8}$$

where n_G e n_0 are the refractive index of the glass and the air respectively, and θ_0 represents the fiber acceptance angle. Considering the silica glass refractive index $n_G = 1.45$, the maximum angle results $\theta_{Gmax} = 8.7°$.

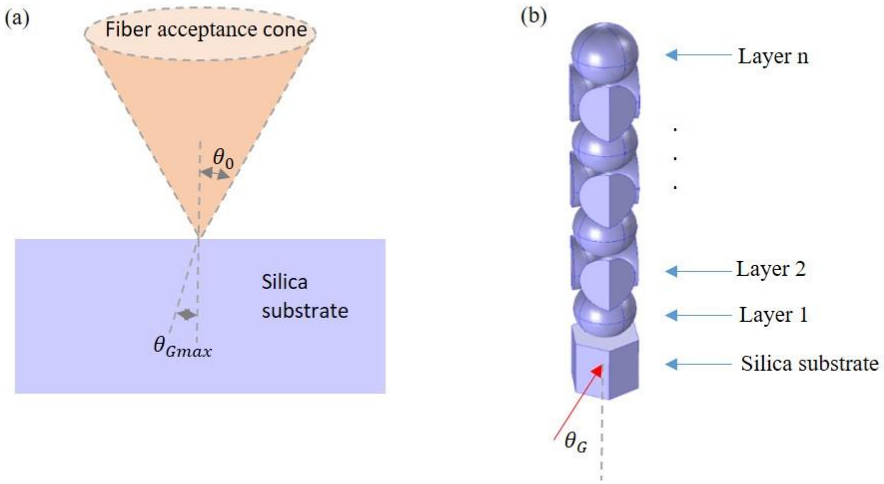

Figure 3. 8. (a) Schematic view of the maximum incident angle; (b) unit cell with incident angle.

Thus, to investigate the effect of the incident angle the reflected spectra of the unit cell were calculated as function of the incident angle θ_G ranging from 0 to 9°.

The Figure 3. 9 shows the reflectance spectra vs the incident angle: it can be observed by increasing the incidence angle up to 9°, a maximum reduction of the peak amplitude of 8.1% and a maximum blue-shift of the bandgap wavelength of 6.0 nm without deteriorate the shape of the spectra. According to these results without loss of generality, in the following analysis we have considered only the normal incidence in order to simply the computational effort.

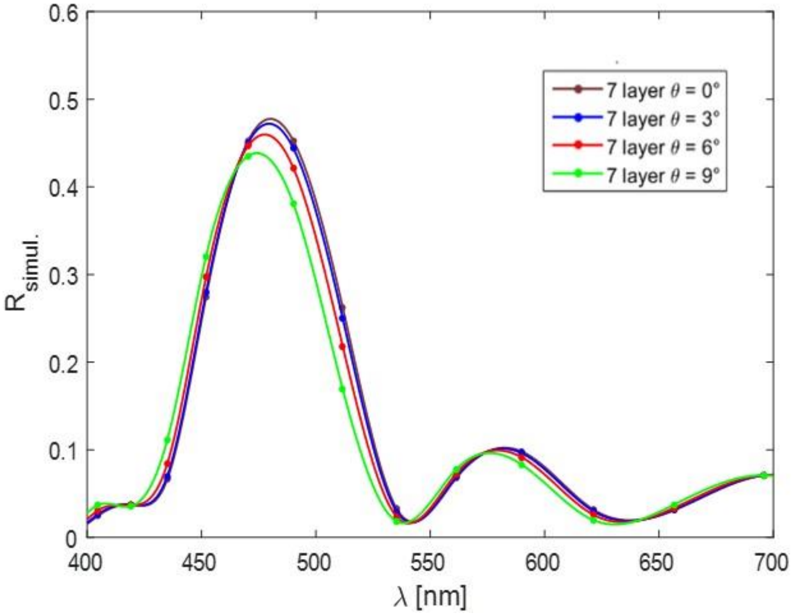

Figure 3. 9. Spectra for different electromagnetic field incidence angles

The results show trivial influence of the input beam incident angle on the reflectance spectrum, except for a bandgap wavelength blue shift of maximum 6.0 nm with increasing incident angle. This means that the numerical results, obtained with the simplest plane wave orthogonally incident to the silica surface, are valid for predicting the experimental behavior and for acting as design criteria tool, except for a little approximation in the bandgap wavelength.

Dependence on nanospheres diameter.

In this section, the dependence of the reflectance spectra on the nanospheres diameter is numerically investigated. The results, shown in Figure 3. 10 (a), point out that by increasing the diameter, a red-shift in the spectra will occur. This behavior is quasi-linear with a slope of 2.43 nm/nm, as summarized in Figure 3. 10 (b), whereas a trivial change in the maximum peak amplitude is appreciated.

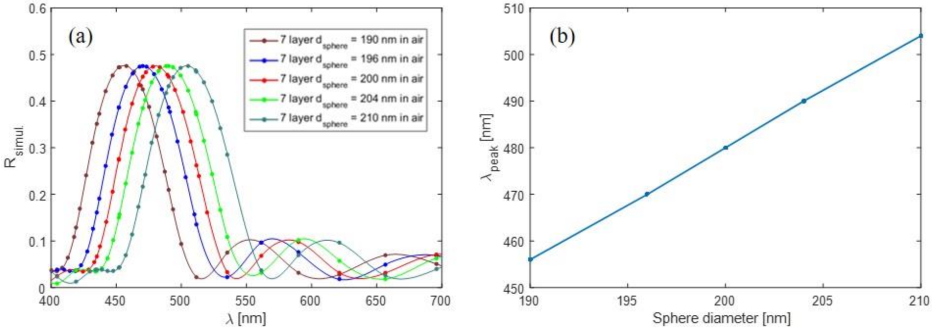

Figure 3. 10. (a) Numerical reflection spectra for different nanospheres diameters; (b) bandgap wavelength vs nanospheres diameter.

This result shows that the nanospheres diameter represents an efficient tool to tune the bandgap wavelength. It also could represent a valid sensing approach to sense any analytes or chemicals able to induce nanospheres swelling.

Dependence on nanospheres refractive index.

Figure 3. 11 (a) shows the variations of the reflectance spectra by changing the refractive index of the nanospheres. The increase of the spheres refractive index induces a red-shift of the bandgap wavelength with linear behavior of 250 nm/RIU, as shown in Figure 3. 11 (b). Additionally, the spheres refractive index also acts on the resonance peak amplitude due to the increment of the refractive index difference between polystyrene spheres and external material.

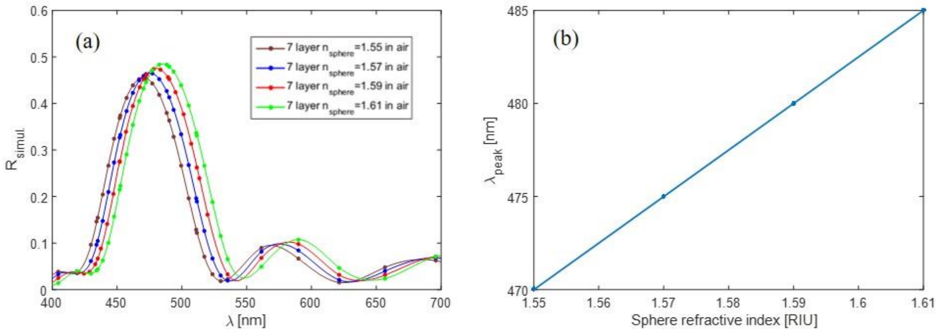

Figure 3. 11. (a) Numerical reflection spectra for different nanospheres refractive indices in air; (b) Bandgap wavelength peak vs nanospheres refractive index.

Dependence on external refractive index.

One of the most appealing feature of the CC, useful in chemical sensing application, is the surrounding refractive index (SRI)

dependence of the spectral characteristics. To this aim, the Figure 3. 12 (a) shows the numerical reflectance spectra for different SRI values. The main relevant effect is an appreciable red-shift of the resonance wavelength with SRI increasing.

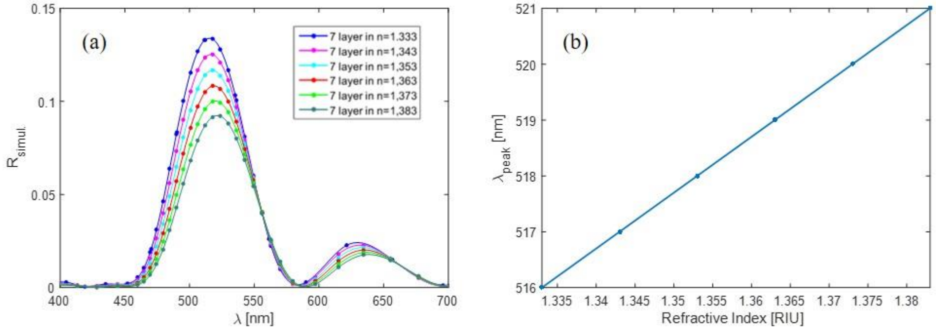

Figure 3. 12. (a) Numerical reflection spectra for different external refractive index values; (b) bandgap wavelength vs external refractive index.

The resonance wavelength peak shift is linear with a sensitivity of 100 nm/RIU as shown in Figure 3. 12 (b). Moreover, when the SRI increase, since the 3D dielectric contrast decreases, the peak amplitude decreases as well.

Refractive Index Sensitivity

Since the bandgap behavior of colloidal structures is strongly dependent on the contrast of dielectric periodicity, significant surrounding refractive index (SRI) sensitivity is expected [83]. To assess the sensitivity of the proposed fiber probes to SRI, reflectance spectra were measured while the optical fiber probes were immersed in different solvents with known refractive index. To this aim, several probes were selected to investigate the repeatability vs dipping procedure and fiber cutting with good results.

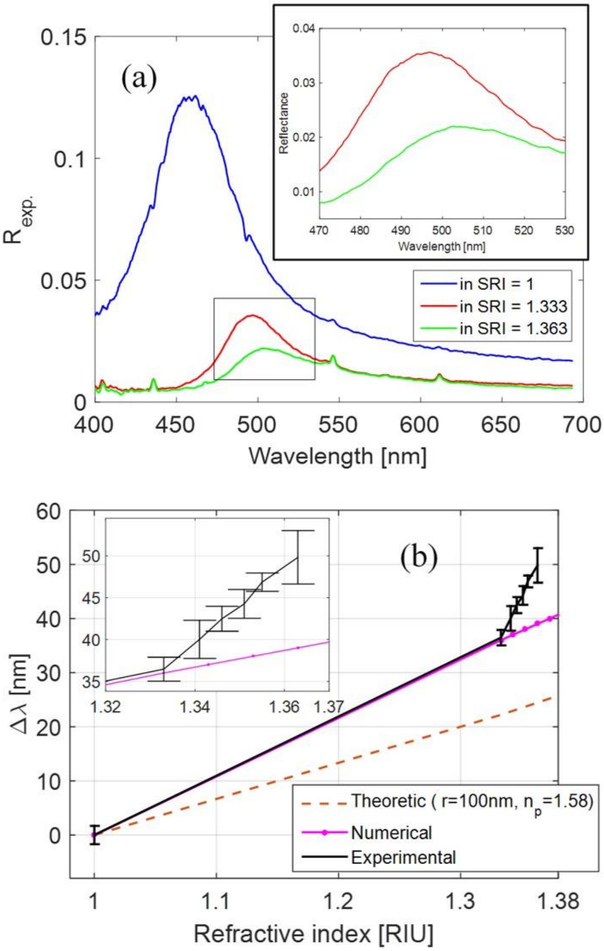

Figure 3. 13. (a) Experimental spectra for different surrounding refractive index; (b) experimental and numerical data vs different surrounding index.

In Figure 3. 13 (a), the experimental spectra of a selected sample for different SRI ranging in 1-1.363 are shown. The main effect is a significant red-shift of the bandgap wavelength combined with a modification of reflectance amplitude and peak visibility.

In Figure 3. 13 (b) the bandgap wavelength shifts of the experimental and numerical data versus SRI are compared. So as to confirm the experimental behavior, reflectance spectra as function of SRI were evaluated by taking into consideration different (more than 20) fiber probes fabricated in the same condition and by taking into consideration different surrounding media. Thus, the experimental data are plotted taking the average values of all tests whereas the standard deviation ranging from 1.1 nm for SRI = 1.355 to the maximum value of 3.2 nm for SRI = 1.363 was plotted by means of error bar. It is worth highlighting that when the external medium changes from air to water (SRI moves from 1 to 1.333) the experimental and numerical data are in very good agreement exhibiting a wavelength shift of 36 nm (Sensitivity of 108 nm/RIU). Concerning the experimental data, further increases of the SRI induce significant enhancement of the SRI sensitivity up to 445 nm/RIU. In contrast, the numerical SRI sensitivity keeps unchanged.

A complete understanding of the difference between numerical and experimental data has not yet attained. However, our experimental shift is in very good agreement with resonance shift of the planar 3D self-assembly structures presented in [83]. Indeed, they investigated polystyrene nanospheres with diameter of 230 nm achieving a red shift of 55 nm as SRI moves from air (SRI=1) to ethanol (SRI=1.363), in perfect agreement with our shift taking into consideration a scaling coefficient due to nanospheres size. As matter of fact, the penetration of air void with water and then with high refractive index materials caused a wavelength shift higher than numerical one which could be attributed to the swelling of the PS nanospheres [83].

Moreover, in spite of its simplicity in fabrication procedure, the achieved SRI sensitivities are important when compared with alternative fiber probes including more complex configurations based on metal or metallic-dielectric structures [54,61,84]. For instance, an SRI sensitivity of 125 nm/RIU[54] was demonstrated for a hybrid metallo-dielectric nanostructure custom fabricated on a single-mode fiber tip exciting LSPR. Instead, Lin et al. [61] demonstrated an SRI sensitivity of 195.72 nm/RIU by an ordered array of gold nanodots on a single-mode fiber tip. Again, very high SRI sensitivity were recently demonstrated by metal-dielectric crystal fabricated by breath figures approach on fiber tip [85].

Moreover, the figure 20 (b) shows the theoretical wavelength shift derived by first order Bragg reflection by [111] planes of face centered cubic (FCC) structure of the colloidal crystal, widely discussed elsewhere [83,86–88]. The resonant wavelength can be expressed as:

$$\lambda = \left(\frac{8}{3}\right)^{\frac{1}{2}} 2r\left(\phi n_p + (1-\phi)n_m\right) \quad \text{Equation 9}$$

Where ϕ is the filling factor fixed to 0.74 in our geometry, r the radius of the nanospheres, n_p the nanospheres refractive index and $n_m$the refracrive index of the media between the nanospheres.

As evident, it shows a lower SRI sensitivity as compared with numerical and experimental data probability due to the first order approximation. In perfect agreement with data in ref [83] the theoretical shift (vs air value) is 2.6% and 5.3% lower than experimental data for water (SRI=1.333) and ethanol (SRI=1.363), respectively.

Finally, in Figure 3. 13 (a) a decrease of reflectance amplitude in- and out-photonic bandgap range with increasing SRI is clearly evident. In effect, the increase of SRI induces a decrement of the dielectric contrast of the colloidal structure and a decrease of the discontinuity between fiber tip and average external medium acting on the in- and out- band reflectance respectively.

3.5 Humidity sensitive photonic crystal hydrogel

A low-cost humidity sensing material was developed by combining the intrinsic humidity sensitivity of hydrogel, the structure of photonic crystal PhC and the fiber optic technology.

The idea is to design and fabricate an optical humidity sensor using colloidal polystyrene (PS) nanospheres (Aldrich, 10% w/w, 200 nm) beads and a polyacrylamide hydrogel as sensing system, self-assembled on the tip of a UV multimodal optical fiber.

This structure possesses a stopband can be reversible changed in response to external stimuli because the PhC are coupling with hydrogel, materials formed by networks of crosslinked hydrophilic polymers that retain around 30% in weight of water.

The swelling behavior of the hydrogel in the presence of water led to an increase of the distance between the latex spheres and consequently a shift of PhCs' stopband (Figure 3. 14).

Figure 3. 14. Schematic illustration of the period structure change of the PhC hydrogel in two different humidities conditions.

3.5.1 Materials and Procedure

Materials.

Acrylamide (AAm) was purchased from Acros Company; N,N'-methylenebis(acrylamide) (BIS) from Fisher Scientific. The photoinitiator (Irgacure 2959) was purchased from BASF. Monodispersed polystyrene (PS) beads (aqueous dispersions, 10% w/w) with a 200 nm diameter were purchased from

Sigma Aldrich (Italy) and used as received. All the chemicals were used with no further refinement.

Preparation of the hydrogel on the tip of the fiber

An UV-VIS multimode fiber optic, 200 µm core (Thorlabs, U.S.A.) was cut by using a high precision cleaver (Fujikura, Tokyo), and successively dip-coated from a colloidal water PS suspension (Sigma Aldrich), by means of an automated system (NIMA Technology Micro-Processor Interface IU4, Spain) at a vertical immersion/extraction speed of 107 mm/min.

The solution to obtain the hydrogel were prepared mixing the monomer (AAm, o,5g), the cross-linker (BIS, 0,012g) and the photoinitiator (Irgacure, 0,012g) in 2 mL of distilled water. After the preparation of the stock solution, the deposition of hydrogel was achieved by dipping the optical fiber tip coated with PS beads into the hydrogel solution, then a light from a xenon lamp was launched through the optical fiber. The UV light is launched for 30 minutes.

3.5.2 Morphology Characterization

An Olympus BX51 optical microscope was used to show the color and the morphology of the film on the fiber tip. To ensure the presence of the nanostructure on the tip, an image of the clean fiber is reported (Figure 3. 15).

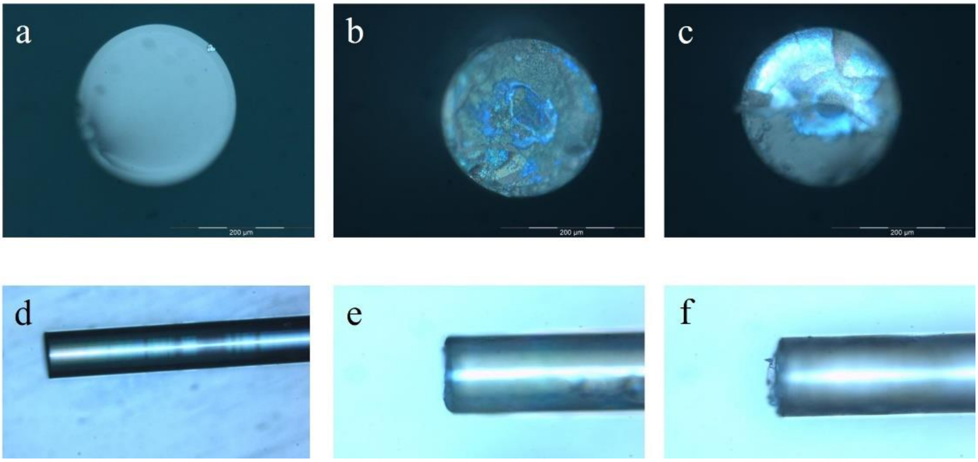

Figure 3. 15. Digital photos of the as-prepared fiber optic sensors. Cross (a-b-c) and lateral (d-e-f) section of (a) bare fiber (b) PS nanoparticles and (c) PS nanoparticles infiltrated with acrylamide solution on the fiber tip.

The presence of the photonic crystals structure was clearly perceptible in the blue-green color show in Figure 3. 15.

A scanning electron microscope (SEM) was used to investigate the morphology of the surface of the photonic crystal on the tip of the optical fiber.

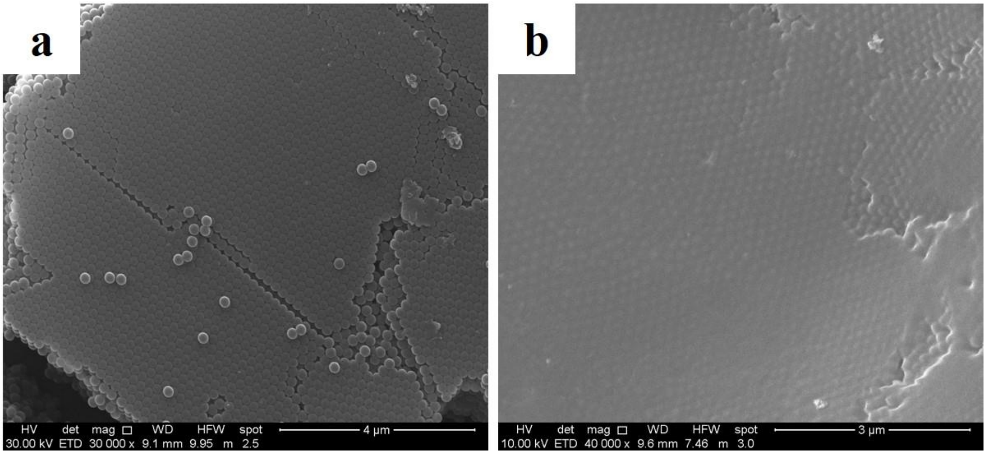

Figure 3. 16. SEM images of the PhC on the tip of the fiber. (a) PS PhC (b) PS PhC hydrogel.

Figure 3. 16 (a) presents a typical top view images of the PhC on the fiber tip, the image indicate that the colloid spheres are in face-centered cubic arrangement. In contrast, Figure 3. 16 (b) shows a typical top view SEM micrograph of the PhC hydrogel, the surface seems to be covered which implies that part of the polyacrylamide hydrogel has been deposed at surface of the latex spheres and another part of the hydrogel has been infiltrated into the voids between the nanoparticles.

3.5.2 Relative humidity measurements

In order to evaluate and measure the wavelength shift under different humidity, several salt solutions of desired relative humidity were prepared and allowed to equilibrate in a closed container at room temperature: 10% RH, KOH; 30% RH, $MgCl_2$; 70% RH, NaCl, 85% RH, K_2SO_4. For the RH 100% the fiber optic tip was immersed in liquid water. In addition, a commercial electronic hygrometer (Honeywell HIH-4000 Series) and resistance temperature (PT-100) detectors have also been used to test the salt solutions.

The fiber coated by PS beads and hydrogel was placed inside the humidity chamber for 80 minutes, and the corresponding reflection spectrum are recorded by a UV-Vis spectrometer. (for more details about the set-up measurement see Appendix – IV Optoelectronic set up).

The schematic illustration of the experimental set up is reported in Figure 3. 17.

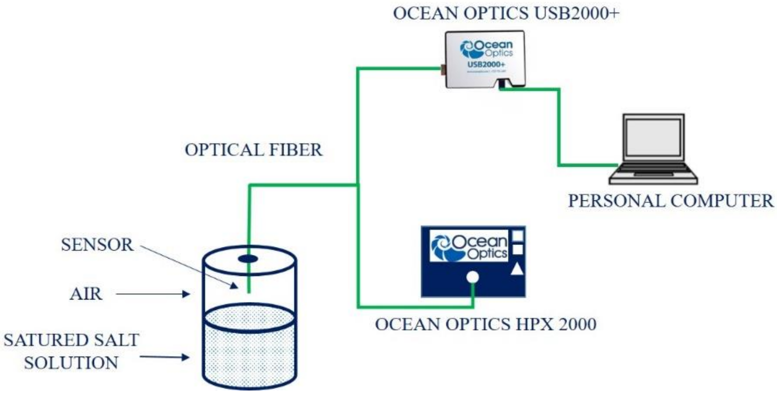

Figure 3. 17. Schematic illustration of reflection spectra experimental set up for the optical fiber tip humidity sensor.

The corresponding diffraction wavelengths of the same sample were recorded every 1 minute to track the peak shift when the sensor was placed in a new humidity environments. In addition, the same experiment conditions were repeated 5 cycles on the same sample to demonstrate the stability and the reproducibility of the sensor.

Figure 3. 18 illustrates the change in reflectance as the relative humidity (RH) varies from 30% to 90%. The peak reflectance of the PhC hydrogel at 30% lies at 470 nm, when the RH is increased to 90%, the peak in reflection increases to 498 nm.

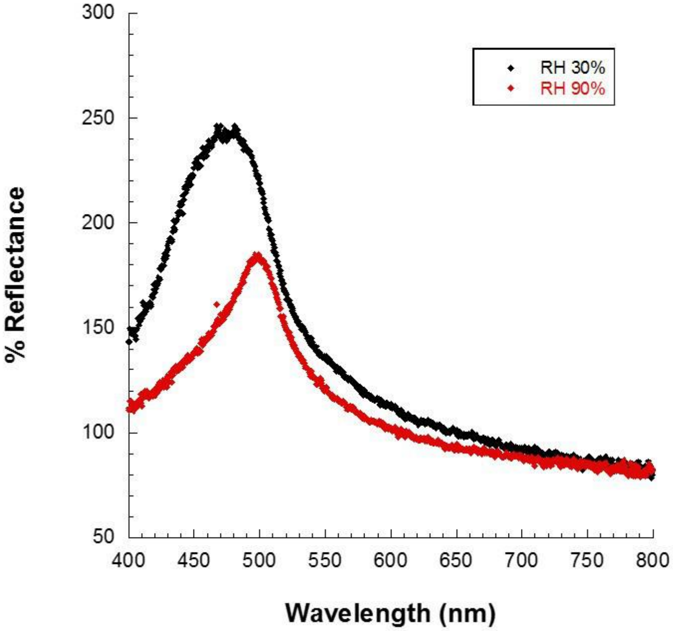

Figure 3. 18. Reflectance spectra of optical fiber sensor under low (30% RH) (dark line) and high (90% RH) (red line) humidity conditions

Figure 3. 19 shows the time dependence of the change of the peak position of the photonic humidity sensor as the humidity increase from air (57%) to 90% and falls back to air in which we can see that the diffraction wavelength immediately begins to shift after a few minutes when the relative humidity changes.

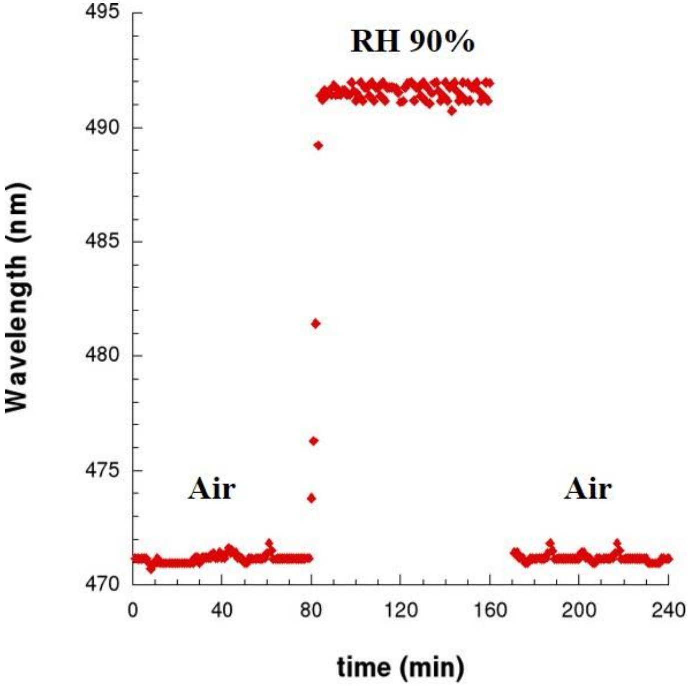

Figure 3. 19. Peak position shift with time under different humidity conditions. At t=50 minutes the fiber optic sensor is in a closed chamber at RH 90%, the fiber is removed at 200 minutes and the sample returns to room conditions.

In order to test the stability of the photonic humidity sensor and the reproducibility of the reflection signals, the same experimental conditions were repeated 5 times on the same sample and the corresponding diffraction wavelengths were all recorded and show in Figure 3. 20.

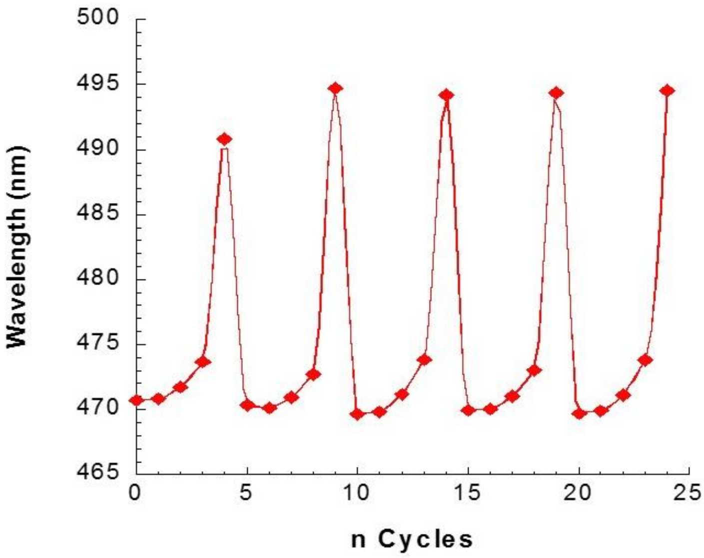

Figure 3. 20. The reversible change in the diffraction wavelength of the photonic humidity sensor in 5 continuous cycles as the humidity switches between 10% and 100%.

In the figure above, it is possible to see that the diffraction wavelengths of each cycle are very close to each other, which demonstrates that the sample presents good stability and reversibility during 5 continuous cycles as the RH switches between 10% and 100%.

3.6 Conclusions

This chapter can be divided in two main part. In the first part the possibility to realize a photonic bandgap structure involving a self-assembly colloidal crystal CC directly on the fiber tip surface with very simple procedure has been investigated. Polystyrene nanospheres with 200 nm diameter and UV-VIS optical fiber with core diameter of 200 µm has been considered. 3D highly ordinated structures have been fabricated on the optical fiber tip from a commercial monodisperse PS beads water suspension. The effectiveness of the patterning approach is clearly demonstrated by the SEM analysis.

The fiber optic probe exhibits a clear resonant peak in the reflected spectrum that is the signature of the formation of a photonic bandgap structure. Despite the simplicity and the low cost of the fabrication procedure, a good repeatability has been obtained for both the resonant peak wavelength and amplitude. The experimental spectra are in good agreement with the results of a model that accounts for a photonic crystal structure confirming the realization of an ordered and controlled geometry on the fiber tip. In addition, the possible sensing mechanisms can be also enlarged by considering that the spectral features of the photonic crystals are linked, not only to the refractive index of the filling phase, but also to the structural parameters of the lattice (particle dimensions and spacing between the particles) and to the refractive index of the particles themselves.

In the second part, a proposed sensing probe for chemical sensing has been reported. A humidity sensitive PhC hydrogel was facilely fabricated by combining the intrinsic humidity sensitivity of polyacrylamide gels, the photonic crystal structure of polystyrene beads and the fibre optic. The results would provide a new insight into the design and development of novel composite functional materials based on a PhC template.

4.

Label-free optical biosensing at sub-femtomolar detection limits [2]

4.1 Abstract

Real-time monitoring of specific biomolecular interactions has attracted a great deal of interest in the last few years. For this application, many label-free techniques have been developed. However ultra-low-concentration quantitative analysis is still challenging. In this chapter, we developed a highly sensitive biosensor based on functionalized photonic crystal (PhC) immobilized on the tip of an UV-Vis optical fiber. We evaluated the performance of the biosensor using a standard streptavidin-biotin binding system. A streptavidin immobilization strategy on the polystyrene beads sensing surface is herein proposed. Real time detection of biotinylated Bovine Serum Albumin (bBSA) molecules has been achieved. The PhCs, generated by the regularly nano-patterned high refractive index spherical regions are sensitive to small changes of refractive index. Therefore, functionalized PhCs have been proven to be a powerful tool for detection of biological species,

---

[2] *This chapter is partially adapted from the following article: L.Sansone, E. Macchia, C. Taddei, L. Torsi, M. Giordano. Label-free optical biosensing at sub-femtomolar detection limits. To submitted.*

down to sub-femtomolar detection limits. Finally, control experiments proving the selectivity of the biosensing platform have been conducted as well.

4.2 Materials and Procedure

Materials.

Monodispersed polystyrene (PS) beads (aqueous dispersions, 10% w/w) were purchased from Sigma Aldrich (Italy) and used as received. The particles have a nominal diameter of 200 nm. Streptavidin (SA), Bovine Serum Albumin (BSA) and biotinylated Bovine Serum Albumin (bBSA) were purchased from Sigma Aldrich (Italy) and used with no further refinement.

Particle deposition

An UV-VIS multimode fiber optic, with a core of 200 ± 5 µm in diameter and cladding of 225 ± 5 µm (FG200UEA, Thorlabs, USA, Thorlabs, USA) was cut by using a high precision cleaver (Fujikura, Tokyo), and successively dip-coated by immersion into a colloidal water PS suspension (10% w/w), by means of an automated vertical immersion/extraction operating at a speed of 107 ± 0.1 mm/min (NIMA Technology Micro-Processor Interface IU4, Spain). The three stages of the dip-coating process are reported in Figure 4. 1. At first the tip is immersed into the PS water colloidal dispersion and then the tip is extracted. The PS layer is allowed to self-assembly by slow solvent evaporation.

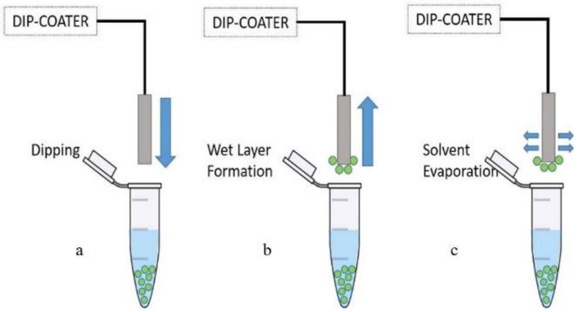

Figure 4. 1. Scheme of dip coating assembly.

The scanning electrode microscope (SEM) images reported in Figure 4. 2 show the regular structure of the adsorbed beads.

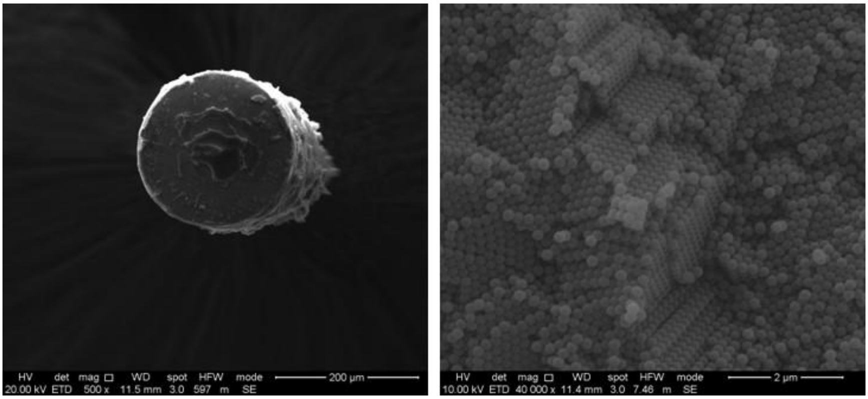

Figure 4. 2.SEM micrographs of a UV-VIS multimodal optical fiber tip surface after the nanobeads adsorption are shown at different level of magnification. The bar set at 2 µm allows to clearly see the periodic structure formed by the self-assembly of the beads on optical fiber tip.

4.3 Spectral Characterization

Reflectance measurements were carried out by illuminating the fiber tip with a xenon optical source (OceanOptics HPX-2000 185-2000nm) and redirecting the reflected light (via a 2 x 1 splitter) to an optical spectrum analyzer (OceanOptics, HR 2000+) by means of a 3dB directional coupler (for more details see Appendix-Optoelectronic set up).

In Figure 4. 3 the reflectance signal of the UV-vis optical fiber is compared to that of a PS modified tip measured in air, in water and in a phosphate buffer solution (PBS, 20 μM, pH = 7). In all these spectra, the elicited spectral feature peaked in the visible regime, characteristic of the PhC generated by the self-assembly of the PS beads, is clearly evident. The acquired spectra are then automatically filtered and elaborated by a MATLAB script that provides the central resonance wavelength (λc) of each spectrum. λ_C, that falls at 455.76 ± 0.48 nm when the fiber is held in air, shifts to 495.58 ± 0.44 nm when it is immersed in water. It is worth noting that no relevant shift is observed, as compared to water, when the tip is immersed in a PBS (495.52 ± 0.50 nm). This is an important aspect as the pH and ionic strength of the PBS are comparable to those of many physiological fluids.

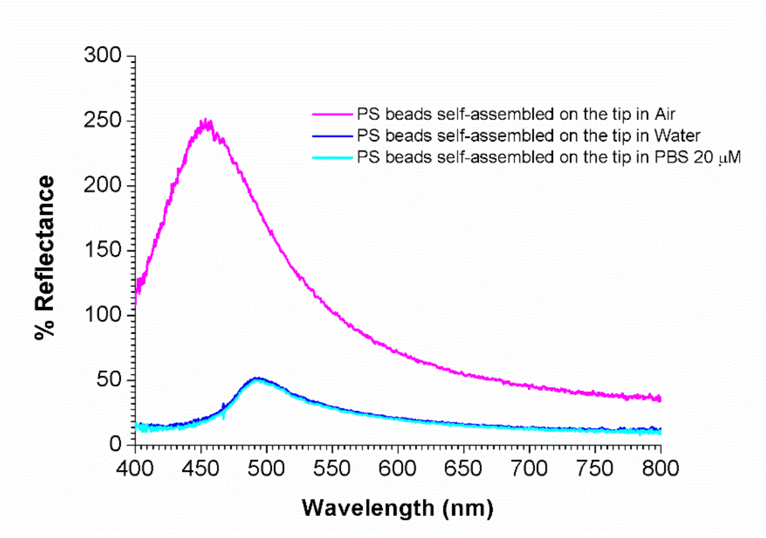

Figure 4. 3. Reflectance spectra of PS beads self-assembled on the tip carried out in air (magenta solid line), water (blue line) and PBS 20 μM (light-blue line).

As already mentioned before the resonance wavelength is determined by the periodicity and refractive index of the assembled PS beads structure, so if the refractive index changes, the wavelength or equivalently reflection color is altered in turn. This is the detection principle that governs the optical fiber sensor platform under study that can be used to detect ligand – receptor interactions, by the changes induced, upon the complex formation in the PhC refractive index and this results in a wavelength shift of the reflected light.

4.4 Fiber functionalization and dose response measurements

Highly sensitive label-free and real-time measurement of the streptavidin - biotinylated bovine serum albumin (SA – bBSA) highly selective interaction was performed by tracking the shift of UV-vis reflectance band upon selective binding. It is, in fact, known that SA and biotin form a very stable complex with dissociation constant in the fM range [89]. The optical fiber tip coated with PS beads was at first immersed in a phosphate buffer solution (PBS) for 120 s. Afterwards, SA was let to deposit on the PS beads surface, by dipping the fiber into a solution 164 nM of SA for 180 min. This step allows the SA molecules to attach to the PS surface by physical adsorption. This is known for being a process leading to stable bio-functionalized PS surfaces [90]. The fiber tip was then rinsed in PBS to remove unbounded proteins on the surface. The tip reflectance spectrum and the relevant peak shift was measured before and after the SA adsorption. The resulting difference accounts, quantitatively, for the of SA adsorbed on the PS beads. To minimize the non-specific adsorption, the fiber tip was dipped into 1.50 fM BSA phosphate buffer solution for 10 min and then rinsed with PBS. This procedure minimizes the adsorption of species that are not the target analyte that selectively interacts with the biological recognition element already attached to the tip surface. At this point the fiber was exposed to concentrations of bBSA ranging from 150 to 1.5 10^7 aM and washed in PBS, before each new exposition. Specifically, measurements were carried out as follows. The PS fiber was incubated for 10 min in PBS and then the reflectance spectrum was registered. The relevant central resonance wavelength provided the *base-line* value (λ_0). Afterwards, the PS fiber was dipped into a 150 aM bBSA PBS solution and incubated for 10 min to allow the complex formation to be accomplished. After rinsing in PBS to remove unreacted excess, the reflectance spectrum was measured again. The relevant central resonance wavelength was taken as the *signal* value (λ) at a given bBSA concentration. The PS fiber was then exposed sequentially, to all the concentrations in the range to be inspected and the relevant λ values were collected. The normalized central resonance wavelength response has been evaluated as:

$$\frac{\Delta\lambda}{\lambda_0} = \frac{\lambda-\lambda_0}{\lambda_0} \qquad \text{Equation 10}$$

where λ and λ_0 are the elicited *signal* and *base-line* value.

As negative control experiment, the elicited measurements were performed with the PS beads functionalized with bare BSA and exposed to bBSA at increasing concentrations, exactly as for the sensing experiment. As the BSA does not selectively binds to bBSA, a signal comparable to the sole non-specific adsorption is to be expected in this case. The data reported in Figure 4. 5 are the relevant to three measurements acquired on different devices and are reported as the average values along with the relevant one relative standard deviations (RSDs).

4.5 Results and Discussion

To demonstrate a proof-of-concept of protein detection with a photonic crystal device, the biosensors here proposed has been tasted with the detection of very well assessed binding such as that of biotin and streptavidin. To this aim, biotinylated BSA binding to streptavidin was chosen to demonstrate the device high performance level. This binding has been extensively studied and is a well understood process, and therefore can serve as a model for the detection of proteins. The systematic approach used in this study is illustrated in Figure 4. 4.

As already introduced, the SA have been let to adsorb on PS beads, self-assembled on the tip fiber, by physical adsorption. This has been achieved by incubating the adsorbed SA proteins in bBSA solutions for a fixed amount of time. Protein can be conveniently adsorbed to various surfaces via intermolecular forces such as electrostatic, hydrophobic, van der Waals, hydrogen bonding interactions, or combination of those. The intermolecular forces are highly dependent on environmental condition such as pH, ionic strength, temperature, and surface condition [91]. Blocking of the tip surface that is not coated by SA has to be performed to minimize nonspecific adsorption of off-target biomolecules. This can be done by letting proteins such as BSA to adsorb. To this end, the sensor surface tip was immersed in BSA solution after SA adsorption. Before the immersion in BSA solution, the fiber tip was immersed in PBS buffer for sufficient time to obtain a stable baseline. This was followed by the immersion in the BSA solution in PBS. After equilibrium was achieved, PBS buffer was again used to remove unbound species until a new, stable baseline was achieved. The immobilization of SA on PS beads induces a red wavelength shift of 21.8 ± 3.4 nm with respect to the bare PS fiber. When the tip is then exposed to BSA, no significant further wavelength shift appears (wavelength shift 2.4 ± 1.0 nm).

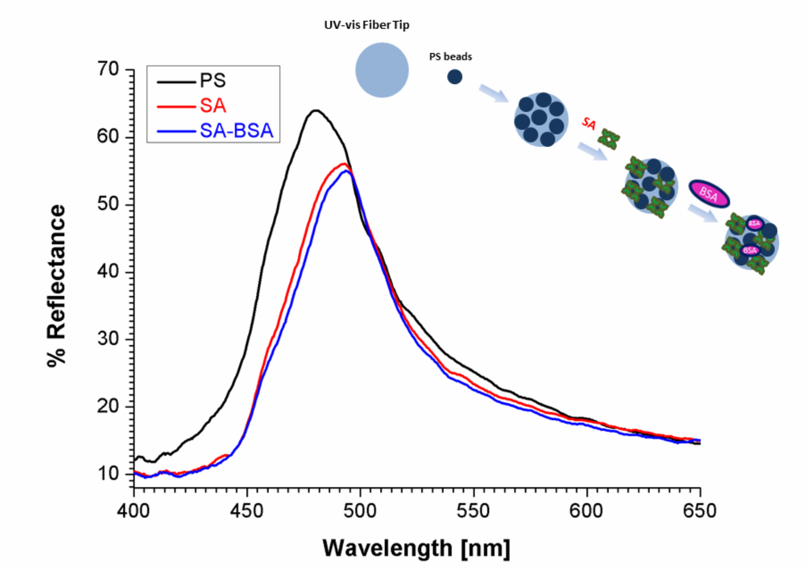

Figure 4. **4.** Reflectance versus wavelength spectra after PS deposition exposed to PBS 20 µM, pH 7 (black line), in PBS after streptavidin (red line) solutions and in PBS after BSA exposure (blue line).

The so prepared tip was immersed in the bBSA solution to evaluate the specific interaction between biotin and streptavidin. After equilibrium, the PBS buffer was again used to remove unbound or weakly attached analyte until a new, stable baseline was achieved. The relative resonance wavelength shift quantitatively compares to the biotin molecules that are bound to the sensing surface, and the result was compared to an independently performed control experiment involving no streptavidin-biotin interaction. The sensor response to the specific binding between the biotin and the streptavidin was related to the size (molecular weight) of the biotin molecule, the immobilized amount of streptavidin on the sensing surface, and the biotin binding sites occupied by the biotin molecule.

In Figure 4. 5 the dose response curves ($\Delta\lambda/\lambda_0$ vs. bBSA concentration of 0.01 pg/mL) of the biosensor relevant to the PhCs functionalized with and without SA are shown (blue and red curves respectively). The responses clearly scale with the logarithm of bBSA concentration. The LOD was estimated as three times the standard deviation of the average response measured in the PBS reference solution (see Figure 4. 5), as 150 aM. Moreover, when the bBSA concentrations increase a red wavelength shift appears. The responses are fast since the protein anchoring only takes few seconds.

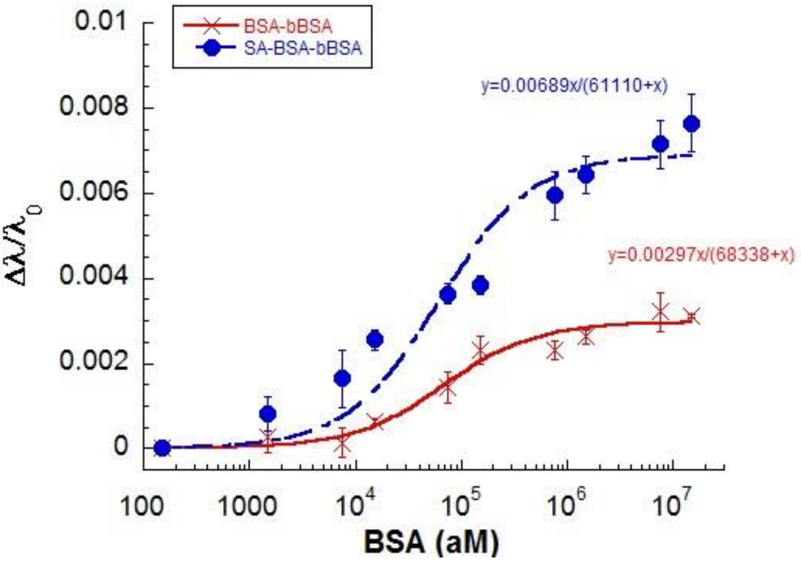

Figure 4. 5. Sensor wavelength vs. bBSA concentration for SA-bBSA system (dots) compared to the negative control BSA-bBSA system (cross).

The Langmuir–Freundlich isotherm for protein adsorption [92] was used to fit bBSA protein adsorption results. This isotherm is given by:

$$B = \frac{B_{max} * F^n}{K_a + F^n} \qquad \text{Equation 11}$$

where B corresponds to bound molecules/μm^2, F denotes the free molecules available for binding, B_{max} is the maximum binding capacity, K_a denotes the adsorption constant for the protein and n is the Langmuir–Freundlich parameter.

The results obtained by this biosensor compared to the other label free biosensors show performances three orders of magnitude better than those reported for the protein detection. Due to miniaturization of the optical tip, this device has potentially high sensitivity, also, for the detection of small numbers of molecules. The sensing area of this sensor is a sub-micron sized area. Binding of just a few molecules at the sensing area generates a signal, which could be detectable by the photonic sensor device. This results in a high sensitivity detection limit. Since the sensing region is the small area at the tip of the sensor, the photonic crystal structure is much less sensitive to environmental perturbation and disturbance.

The approach proposed opens a wider perspective to develop a new label-free optical biosensing for antibodies and proteins, in fact this new system is simple, compact and low cost.

4.6 Conclusions

Future trends in diagnostics will continue in miniaturization of biochip technology toward nanoscale. Our UV-VIS fiber tip based nanochip provides a convenient, low-cost and label-free method for specific and highly sensitive detection of the biomolecular interactions. We anticipate that this technology will extend the limits of current molecular diagnostics and enable point-of-care diagnosis as well as promote the development of personalized medicine. The multiparallel possibilities of biosensing applications have the potential to allow the optimization of biomarker research, cancer diagnosis and also the detection of infectious microorganisms for biodefense.

5.

Magnetic photonic crystal for high sensitivity optical sensor

5.1 Abstract

Nature provides us with a multitude of design solutions finely tuned by natural selection. Biomimetic, ‘‘Learning from Nature’’, allows to find an optimal design to technical applications. Following a recent trend of researches on optical structures in biology, optical biomimetic thrives and yields to various bioinspired optical materials with advanced optical properties mediated by micro and nanostructures borrowed from nature [93]. Optical biomimetic has attracted intensive research interests especially after the identification of photonic crystal. Once the concept of ‘‘photonic crystal’’ was first proposed by *Eli Yablonovitch* in 1980s [1], a tremendous research tide was intrigued due to their great potential for modulating light-matter interaction. However, several years later photonic crystals were discovered in biology like 3D photonic crystals in beetle [94].

Because of the presence of a periodic superlattice of colloids and voids, colloidal crystals (CCs) bear many unique structures and fascinating properties which are distinctly different from those of standard crystals with atoms, ions or molecules as repeating subunits. CCs have attracted much interest over the last two decades,

largely because of their unique photonic properties. The archetype opal structures are based on close packed arrays of spheres of submicrometer diameter embedded into a micron range matrix. Due to the lattice structure of CCs the light with a wavelength matching the lattice distances will undergo the Bragg diffraction to form structural colors and photonic band gaps (PBGs) [95].

The main objective of this chapter is the design, manufacturing and characterization of magnetic responsive photonic crystal (RPC), a structure capable of changing its photonic band gap properties by an external stimulus and simultaneously diffracting brilliant colors under sunlight or indoor illumination. These RPC based visual sensor operates through the changes in the lattice constant and/or refractive index contrast of the crystals, which are typically achieved by introducing a stimulus responsive polymer into the interstices of the colloidal packing. For instance, *Ge et al. 2008* [8], reported a magnetically RPC by using highly charged superparamagnetic Fe_3O_4 colloidal nanocrystal clusters. The colloidal structures with regular interparticle spacing of a few hundreds of nanometers along the direction of the external field, so that, the system strongly diffracts visible light. The diffraction wavelength can be tuned across the entire visible spectrum by simply changing the strength of the magnetic field. The fast and reversible response suggests great potential of these photonic materials in applications such as optoelectronic devices, sensors and color display.

The magnetic composite nanoparticles will be realized by using three different approaches: a miniemulsion batch method comprising either a single or four steps and a microfluidic elongation-flow method.

An emulsion is defined as a two-phase system, prepared by mixing two immiscible liquids, in which small globules of one liquid are dispersed uniformly throughout the other liquid [96]. Nanoemulsion, also known as miniemulsion, refers to an emulsion in which globules (droplets) size is typically in the range of tens to hundreds of nanometers. In order to formulate a stable emulsion, it is necessary to consider well the factors which influence emulsion’s quality. These factors include the choice of a proper set of components (dispersed and continuous phases, surfactant or combination of surfactants etc.) and their respective concentration, the choice of an efficient mechanism that can rupture the bigger droplets into micro- or nanoscale ones and finally the selection of a proper order for adding each component [97]. First, total insolubility between the dispersed and continuous phases is a prerequisite although for practical reasons the dispersed phase may be slightly soluble in the continuous phase. In such situation and in case of non-equal size droplets, the Ostwald ripening phenomenon occurs which is experimentally observed by the growing of the larger particles at the expense of the smaller ones by molecular diffusion across the continuous phase. The driving force of the Ostwald ripening phenomenon is the Laplace pressure difference between small and large droplets. Although suppressing the Ostwald ripening phenomenon can be achieved by several means [98], it is easiest to add in the dispersed phase a molecule (so-called Ostwald ripening inhibitor) completely immiscible with the continuous phase which purpose is to create an osmotic pressure which balances the Laplace pressure.

The second requirement is an excess of an ionic surfactant in the continuous phase characterized by a fast adsorption kinetics so that to guarantee the efficient coating of the new coming surface of the nanoscale droplets during emulsification and to prevent by electrostatic repulsion the shear-induced coalescence [99]. Generally, the surfactant is dispersed in the continuous phase with the form of micelles. When the new droplets are produced, these micelles dissociate rapidly into single surfactant entities to cover the droplet’s surface. The concentration of surfactant must be above the critical micelle concentration (CMC). The third requirement is choosing the proper surfactant, which should not undergo the formation of lyotropic liquid crystalline microemulsion phase. Indeed, systems containing surfactant, water, alcohol and short chain alkane are known to be prone to form these phases [100]. The fourth requirement is using an emulsification method that allows rupturing the dispersed phase into nanodroplets and thus overcoming the Laplace pressure.

Several conventional methods are available for producing nanoemulsions. They can be classified into two categories: high-energy and low-energy methods [101,102]. High-energy methods include energy inputs which are provided by apparatus such as ultrasound generator, high-pressure homogenizer, rotor-stator mixer, static mixer and membrane. By using these emulsification methods, the nanodroplets can be obtained by energy transfer with the presence of surfactant whose function is to decrease the interfacial tension.

Recently, *Souilem at al*. have developed a new concept of reactor/mixer (called RMX®) which was successfully used to produce nanoemulsions whose size can be controlled in the range 30-100 nm [103] The working principle of this pneumatic apparatus is based on the reciprocating flow of a crude emulsion through an abrupt contraction which generates a strong elongational flow, known to be more efficient, in contrast to shear flow, to rupture dispersed phase droplets into smaller ones. Although this apparatus operates at moderate pressure (max 6 bars), conversely to the high-pressure homogenizer, the flow regime through the restriction is highly turbulent and may lead to local heating which might be detrimental for certain applications.

On the other hand, microfluidics is the science and technology of systems that process or manipulate small amounts of fluids (10^{-9} to 10^{-18} liters) using microchannels with dimensions of tens to hundreds of micrometers [104]. After one of the first microfluidic device was reported in 1979 [105], microfluidics strongly attracted many scientists due to its bright potential application. Indeed, several benefits can be pulled out from microfluidic technologies compared to large scale technologies. It includes, among others, the use of less volume of samples, chemicals and reagents reducing the global fees of applications. Many operations can be executed at the same time thanks to their compact size, shortening the time of experiment. They also offer an excellent data quality and substantial parameter control which allow automating the process while preserving the performances.

The current study aims at using a microfluidic version of the RMX® which can synthesize nanodroplets to develop a magnetic nanocomposites particles [106]. These microfluidic devices appear as good candidates to prepare monodisperse polymer colloids and nanoparticles which can be used to construct the synthetic opals (The microfluidic samples were realized in collaboration with the Precision Macromolecular Chemistry group (PMC), Charles Sadron Institute (ICS), University of Strasbourg).

5.2 Materials and Procedure

Materials

In this study, five components were required to prepare a standard polymerizable nanoemulsion: monomer, surfactant, hydrophobic agent as an Ostwald-ripening inhibitor, thermal initiator and distilled water. Specifically, the monomer was styrene (St, 99%); the surfactant was sodium dodecyl sulfate (SDS, 99%), the hydrophobic agent was hexadecane (HD, 99%) and the initiator was potassium peroxdisulfate (KPS) All the reactants were purchased from Sigma Aldrich and used as received.

For the synthesis of hydrophobized magnetite nanoparticles, ferric chloride anhydrous ($FeCl_3$), ferrous chloride tetrahydrate ($FeCl_2 \cdot 4H_2O$), ammonium hydroxide (28-30% NH_3), octane (98%), potassium peroxodisulfate (KPS) and oleic acid (90%) were purchased from Sigma Aldrich and used as received.

The monomer was distilled before use. Distilled water was used throughout all the experiments.

a. Miniemulsion method (four-step)

a.1. Synthesis of Hydrophobized Magnetite Nanoparticles (1st step)

According to ref.[107], the magnetite particles were produced by co-precipitation from an aqueous Fe $^{3+}$/Fe $^{2+}$ solution (ratio 3:2) using concentrated ammonium hydroxide in excess. The particles were subsequently coated with oleic acid.

14.6 g of $FeCl_3$ and 12.0 g of $FeCl_2{\cdot}4H_2O$ were dissolved in 50 mL distilled water. 40 mL of ammonium hydroxide were added rapidly. After the co-precipitation of magnetite particles, oleic acid was added (for quantities see Table 5. 1), and the suspension was heated to 70 °C for 30 min. Then, the temperature was increased to 110 °C in order to evaporate water and excess of ammonium. The black lump-like residuum was cooled to room temperature and washed several times with distilled water. After drying, a powder was obtained.

a.2. Water-Based Ferrofluid (2nd step)

Magnetite powder coated with oleic acid (1.0 g) as synthesized in the step before was added to 6.0 g of octane with hexadecane (3.6 wt.% related to the total amount of octane, magnetite and oleic acid) to form a dispersion of hydrophobized magnetite in octane as carrier medium. This dispersion was added to a solution consisting of 24 g water and SDS (for quantities see Table 5. 1). After mixing for 1 h at 500 rpm, the mixture was subjected to sonication twice for 2 min at 90% amplitude with a Misonix Incorporated Ultrasonic Liquid Processor (U.S.A.) in an ice cooled bath. Finally, the solution was heated at 80 °C for 6 h in order to evaporate the octane while every 30 min approximately 2 mL of water was added to compensate the evaporation of water.

Table 5. 1. Preparation conditions.

Sample	**Oleic acid wt.%[a)]**	**Hexadecane wt.%[b)]**	**SDS wt.%[b)]**
Mag 1	22.2	3.6	1.0
Mag 10	44.4	3.6	20,3

a) Related to magnetite.

b) Related to dispersed phase. The dispersed phase consists of octane, magnetite and oleic acid.

a.3. Styrene Miniemulsion (3rd step)

A styrene miniemulsion was prepared using the following recipe: 6.0 g of styrene and 250 mg of the hexadecane were added to a surfactant solution consisting of 72 mg of SDS dissolved in 24 g of water. After stirring 1 h for pre-emulsification, the miniemulsion was obtained by sonication for 2 min at 90% amplitude in an ice-cooled bath.

a.4. Magnetite-Polymer Encapsulation (4th step)

For the encapsulation of magnetite nanoparticles, the styrene miniemulsion and the water-based magnetite dispersions as obtained above were combined and co-sonified twice for 1 min at 50% amplitude in an ice-cooled bath. Magnetite powder to monomer ratios of 4:1, 2:1 and 1:1 were employed. To start the polymerization, 20 mg of KPS were added, and the temperature was increased to 80 °C. The polymerization was then carried out for 24 h.

The four-step synthesis is shown in Figure 5. 1.

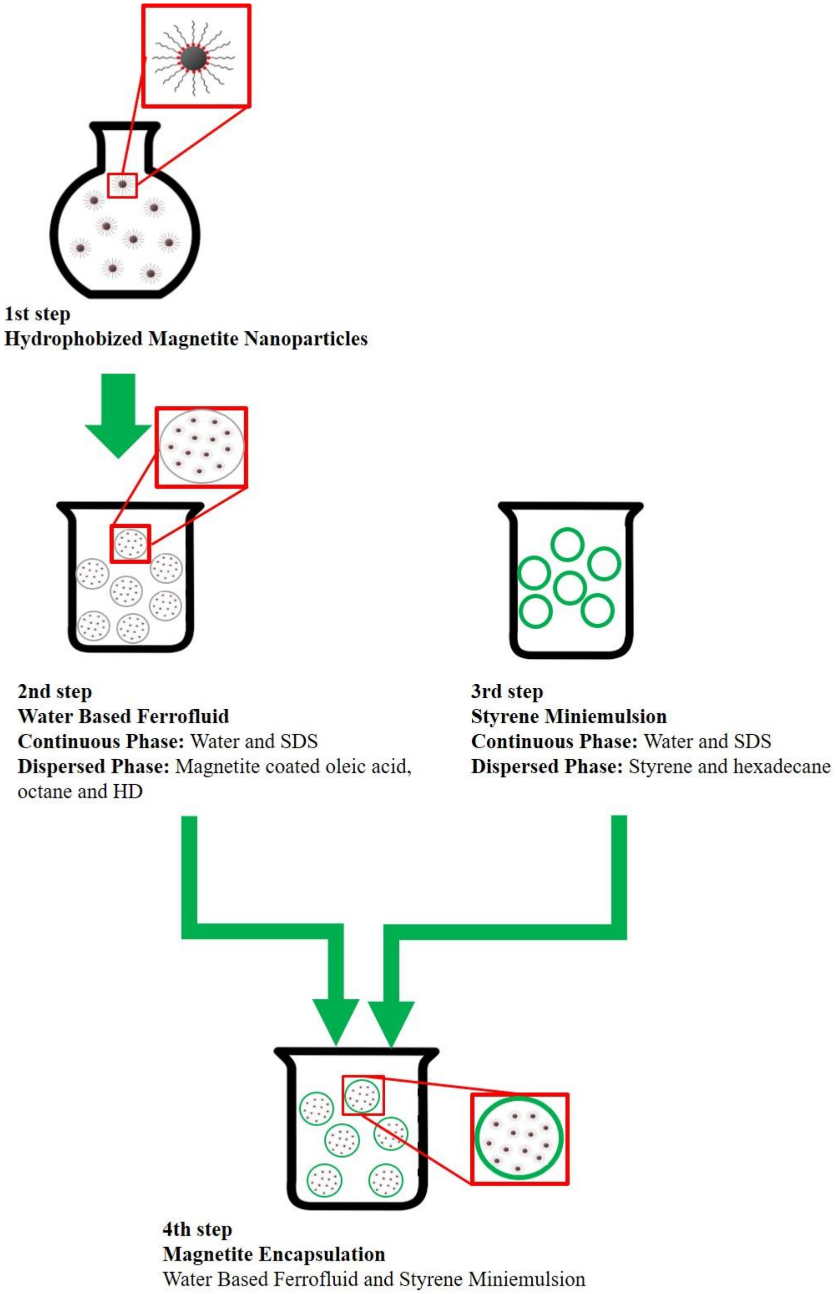

Figure 5. 1. Scheme of preparation procedure of polymer coated magnetite particles. In the first step, dried hydrophobized magnetite nanoparticles are produced and in the second step transferred into an aqueous solution to form a ferrofluid. In the third step a styrene minimeulsion was obtained and then co-emulsified with the water-based ferrofluid from third step (fourth step).

b. Miniemulsion method (One step)

1 g of dried magnetite nanoparticles synthesized in 1st step of miniemulsion method, 1 mL of styrene, 20 mg of KPS as initiator and 40 mg hexadecane were mixed and added to a solution of 8 g water with 12 mg SDS. After stirring for 1 h, the miniemulsion was prepared by ultrasonicating the emulsion for 240 s at 90 % amplitude (Misonix Incorporated Ultrasonic Liquid Processors, U.S.A.) at 0 °C in order to prevent polymerization. For polymerization, the temperature was increased to the reaction temperature of 80 °C. The reaction is usually completed after 4 h.

c. Microfluidic elongational-flow method

As illustrated in Figure 5. 2, the elongational-flow microprocess mainly consisted of two mid pressure syringe pumps (neMESYS Mid Pressure Module, Cetoni), two 25 mL stainless steel syringe (Cetoni) and one PEEK tee (Valco Vici) as the elongational-flow microemulsifier/micromixer. The syringe pumps were operated by the supplier’s software and could independently inject or withdraw, work in tandem (withdraw/withdraw, infuse/infuse) or in opposite phase (withdraw/infuse). The micromixer, in turn, consisted in two drilled microchannels having a bore size of 150 µm. The microchannels were linked to the stainless-steel syringes by two PTFE tubing (1,06 mm ID x 1.68 mm OD).

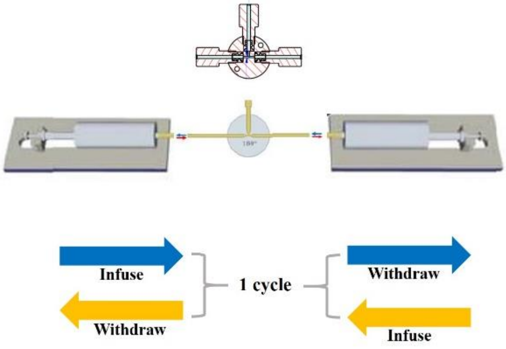

Figure 5. 2. Schematic drawing of the microprocess.

SDS was dissolved in distilled water and hexadecane was dissolved in styrene separately (for more details see Figure 5. 3). Then the two solutions, 4.25 mL of continuous phase (SDS and water) and 0.75 mL of dispersed phase (Styrene, HD, Mag 1 and KPS) were separately charged into one stainless steel syringe for a total volume of 5 mL. Next, the pumps were switched on and forced to operate at the same flow rate and in opposite phase so that the solution passed from one syringe to the other one through the restriction of the micromixer. A back and forth movement of the pump counted for one cycle. The duration of one cycle depended upon the flow rate and the number of cycles. At the end of the procedure, the nanoemulsion was recovered and converted into stable colloidal suspension of polymeric nanoparticles by thermal polymerization. The glass vial containing the nanoemulsion was left overnight in an oven at 70°C.

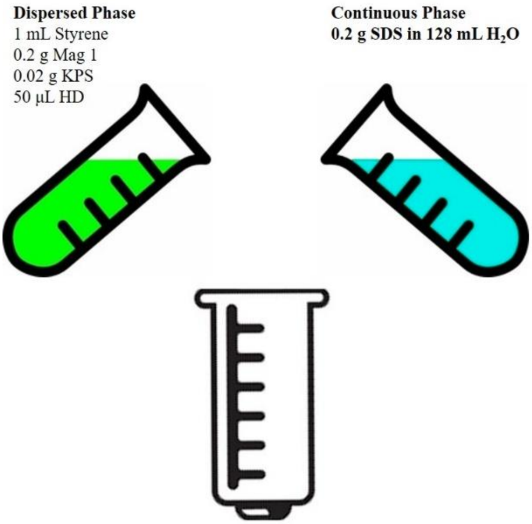

Figure 5. 3. Schematic view of the chemical preparation for the microprocess.

Table 5. 2. Characteristics of the samples consisting of magnetite/polymer particles.

Sample	**Magnetite**	**Magnetite:Monomer**
Latex 1	Mag 10	2:1
Latex 2	Mag 10	4:1
Latex 3	Mag 1	2:1
Latex 4	Mag 1	4:1
Latex 5	Mag 1	Miniemulsion method
Latex 6	Mag 1	2:1 2nd step without HD[a)]
Latex 7	Mag 1	Microfluidic elongational-flow method

[a)] Hexadecane

5.3 Morphology Characterization

Magnetite nanoparticles obtained with two different weight contents of oleic acid were characterized by thermogravimetry (cf. Figure 5. 4). The thermogravimetric analysis (TGA) was performed with a TA-Q500 (TA Instruments Ltd, West Sussex, UK) (for more information see Appendix I - Thermogravimetric Analysis (TGA)).

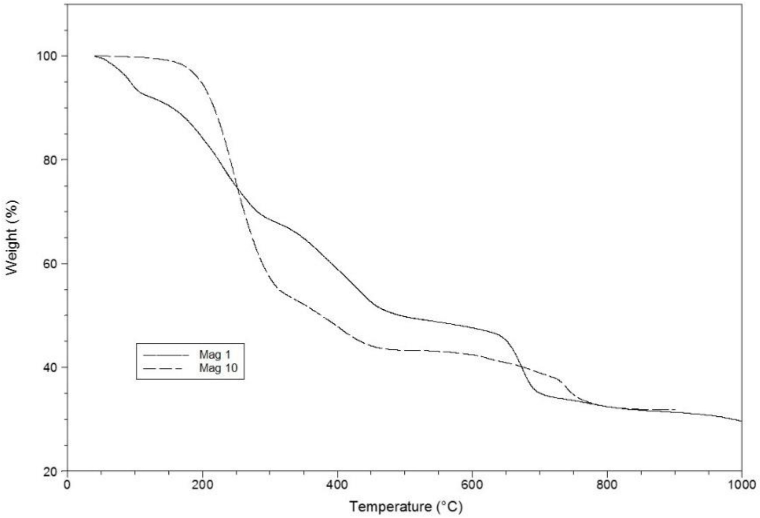

Figure 5. 4. Thermogravimetric curves of magnetite nanoparticles Mag 1 (solid line), Mag 10 (dash line)

In case of the highest weight content of oleic acid (Mag 10, 44.4 wt.% oleic acid) a two-step mass loss was detected. The first mass loss of 45% was obtained between a temperature of 200 and 300 °C, the second mass loss of about 11% was observed between a temperature of 600 and 800°C. This two-step decay indicates that different species of oleic acid were presented in this sample. The first mass loss was attributed to the loss of oleic acid molecules in the outer layer, i.e. the oleic acid molecules weekly linked to the magnetite nanoparticles. The second weight loss was attributed to the loss of oleic acid molecules in the inner layer which is a strongly bound layer between oleic acid and magnetite nanoparticles.

In the case of Mag 1 (22.2 wt.% oleic acid), one step mass loss of 50% is detected between 200 and 700 °C. It is also possible to note a little mass loss of 10% between 600 and 700°C. This second mass loss maybe is due to some non-react oleic acid during the magnetite nanoparticles synthesis.

In Figure 5. 5, the thermogravimetric measurements of Latex 3, Latex 5 and Latex 7 show the same transitions for the samples prepared with different procedures between room temperature and 700 °C. The step loss about 80% is attributed to removal of the polystyrene for all the samples.

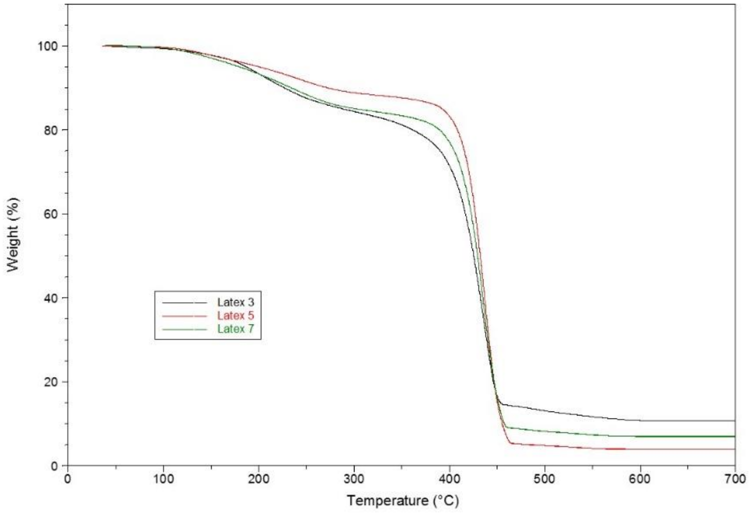

Figure 5. 5. Thermogravimetric curves of samples. Latex 3 (black line), latex 5 (red line) and latex 7 (green line)

The magnetite polymer particles were also characterized by Transmission Electron Microscopy (FEI Tecnai G12 Spirit Twin). In **Errore. L'origine riferimento non è stata trovata.** structural composition of Mag 10 and Mag 1 is observed. In both cases, the particles are roughly spherical or ellipsoidal.

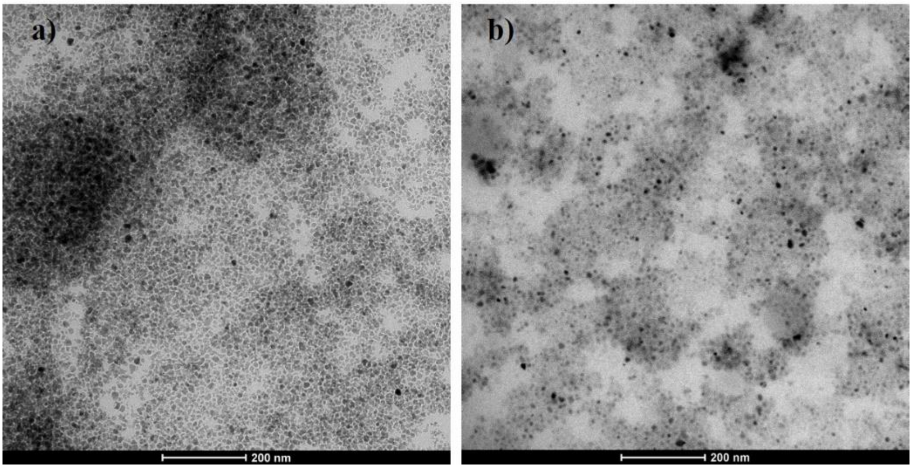

Figure 5. 6. TEM micrographs of Mag 10 (a) and Mag 1 (b).

In Figure 5. 7, the second step procedure is observed for Latex 3 and Latex 4 to show the structural composition of water-based ferrofluid. The second step is crucial for the encapsulation process. The water-based ferrofluid shows a high stability due to a double surfactant layer, one is the oleic acid that provides a hydrophobicity of the particles while the second (SDS) promotes the stabilization in water.

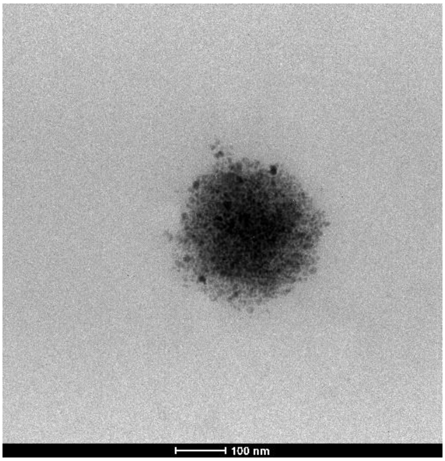

Figure 5. 7. TEM micrograph of water-based ferrofluid (2nd step).

In the fourth step, a monomer miniemulsion is added to the water-based ferrofluid containing the magnetite aggregates. In Figure 5. 8 the Latex 1 and Latex 2 prepared from Mag 10 and a styrene miniemulsion were mixed in a ratio of 2:1 and 4:1. In both the micrographs a good magnetite encapsulation is obtained. Particles with diameters of about 70 nm are found.

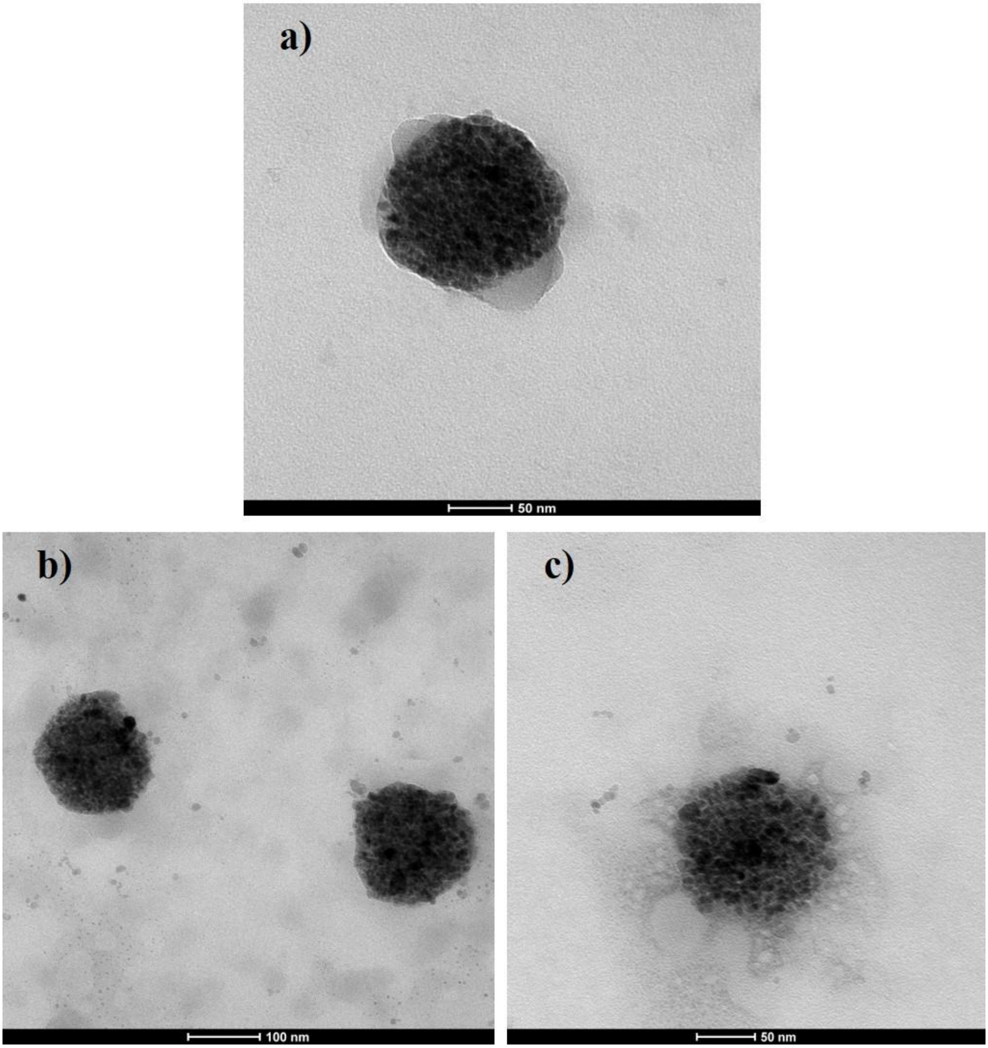

Figure 5. 8. TEM micrographs of Latex 1 (a) and Latex 2 (b-c) at different magnifications.

Figure 5. 9 and Figure 5. 10 present the micrograph of Latex 3 and Latex 4, obtained after mixing Mag 1 and a styrene miniemulsion in a ratio of 2:1 and 4:1 respectively. In all the as-prepared samples a good encapsulation of magnetite nanoparticles is observed but with an inhomogeneous distribution of the diameter of the nanoparticles.

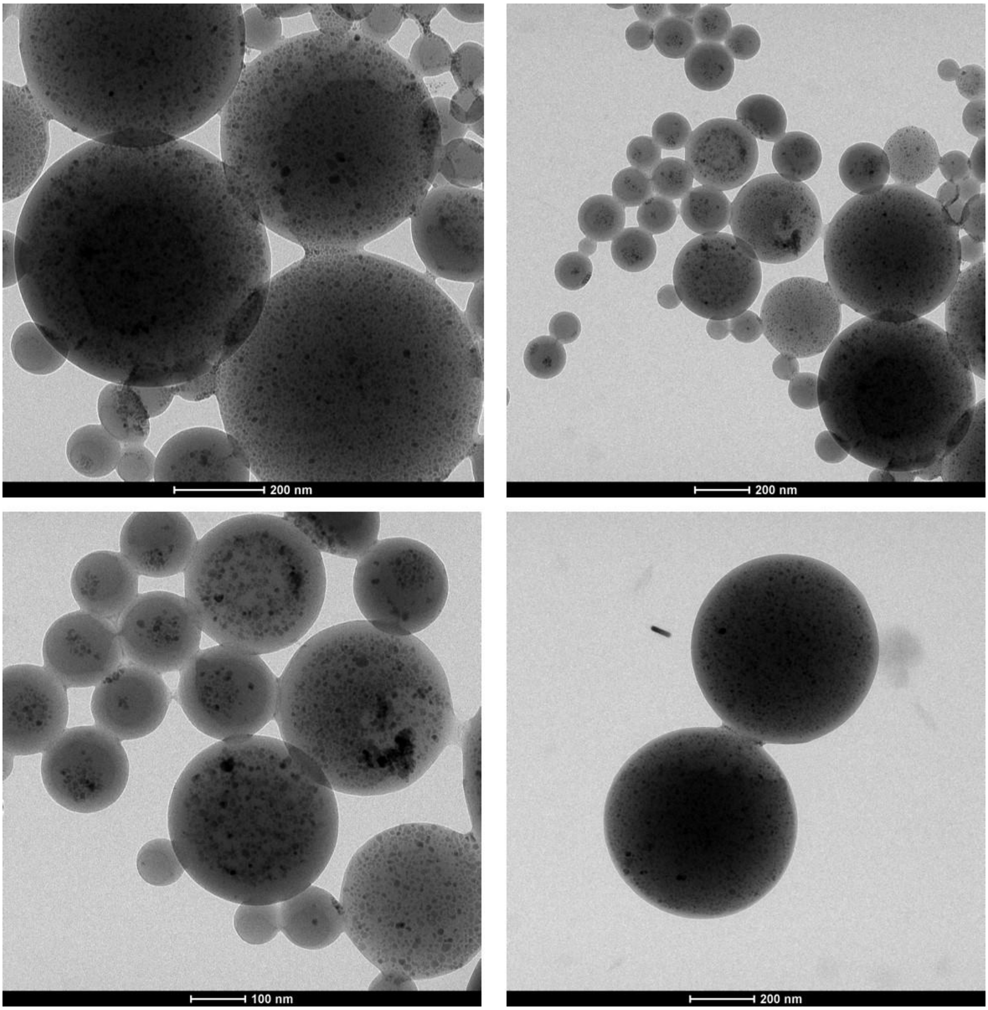

Figure 5. 9. TEM micrographs of Latex 3 at different magnifications.

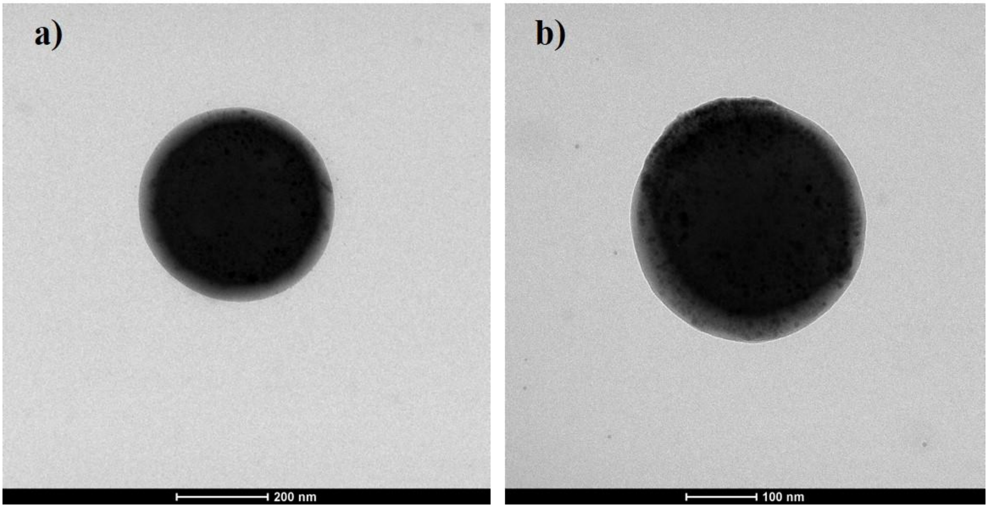

Figure 5. 10. TEM micrographs of Latex 4 at different magnifications.

Figure 5. 11 presents a micrograph of the latex obtained by a one-step polymerization. It is clearly observed that polymer particles with magnetite nanoparticles encapsulated in the polystyrene matrix were attained. Within the polymer particles, the smaller magnetite particles are easily identified and the single magnetite entities seem to be still well separated. The distribution of magnetite seems to be rather inhomogeneous compared to the samples obtained with miniemulsion method with four step, some of them containing large amounts of magnetite, some of them being partially empty of magnetite nanoparticles. Moreover, the resulting particle size of Latex 5 is rather broad compared to Latex 4.

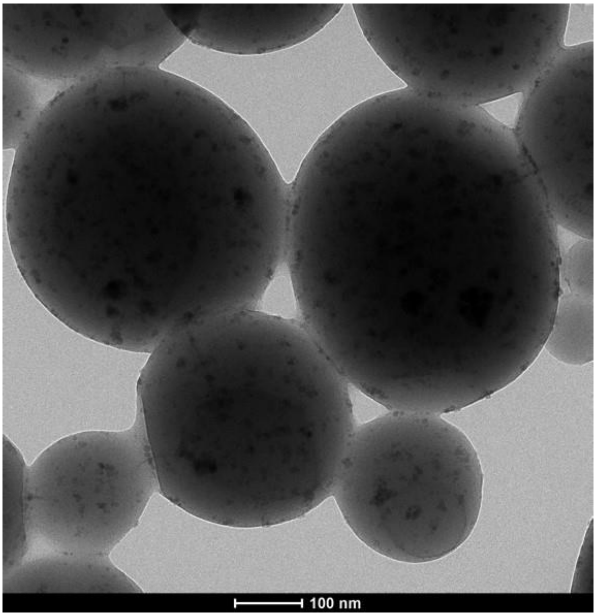

Figure 5. 11. TEM micrographs of Latex 5 obtained by the one step batch miniemulsion method.

TEM micrographs of the sample prepared without hexadecane are presented in Figure 5. 12. Same as Latex 5, it is observed that there are particles with a large amount of magnetite, particles partially empty and there are also some particles broken. This morphology indicated that during the miniemulsion polymerization process without HD, a phase separation occurred lead to a formation of asymmetric particles.

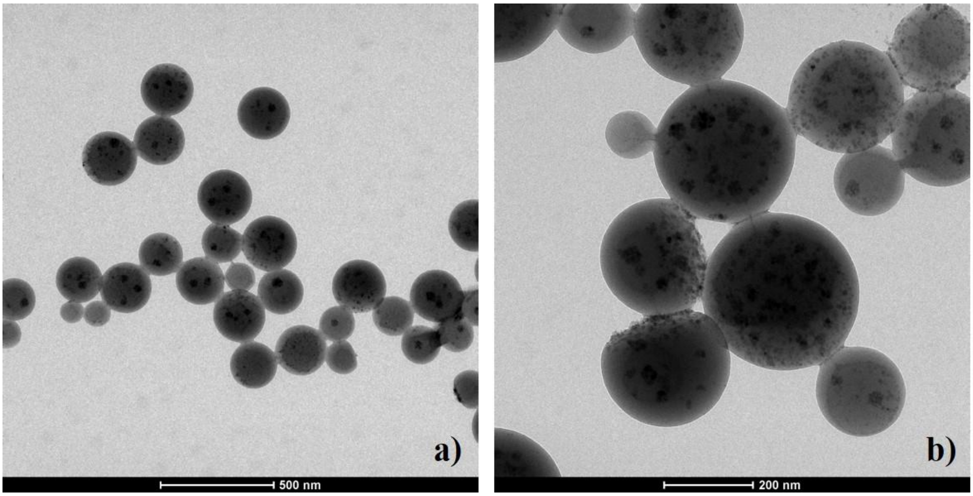

Figure 5. 12. Transmission electron micro TEM micrographs graph of Latex 6 (a-b) at different magnifications.

Figure 5. 13 shows the TEM micrographs of the composite nanoparticles realized by the microfluidic microprocess under the following conditions: the flow rate was set to 30mL/min, 100 cycles and a bore diameter of the micromixer of 0.15 mm.

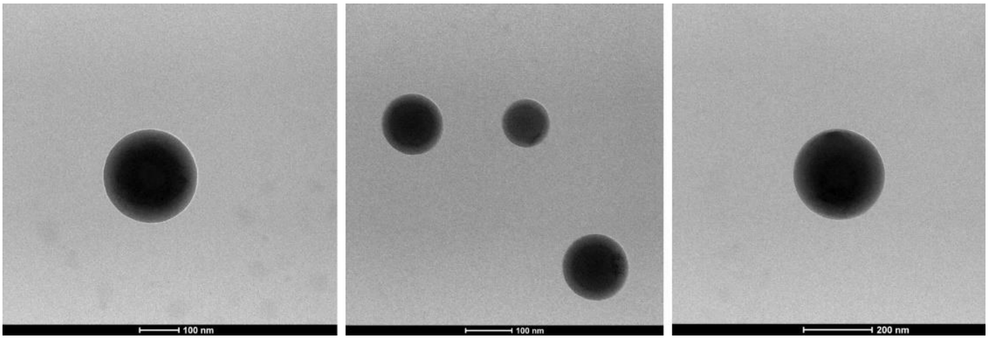

Figure 5. 13. Latex 7 micrographs at different magnifications.

The particles obtained with the microprocess exhibit a narrower size distribution compared to those obtained with the miniemulsion method even.

EDX was carried out at randomly selected areas of sample to find out the atomic distribution. The nanoparticles’ energy dispersive X-ray pattern exhibits iron peak at different weight percentages. Although the sample prepared with the microfluidic process are more uniform in shape, the weight percentage of iron is less than the samples prepared with the miniemulsion method (Table 5. 3). The less magnetite content in the sample prepared with microfluidic process maybe is due to some magnetite nanoparticles that remain in the syringes and in the PTFE tubing.

Table 5. 3. Elemental composition of prepared samples.

Elements	**Latex 3** (wt.%)	**Latex 5** (wt.%)	**Latex 7** (wt.%)
Oxygen	18.48	22.82	21.03
Silicon	67.72	60.21	67.53
Potassium	2.73	2.75	7.41
Iron	8.54	11.25	4.02

The thermogravimetric analysis of Latex 7 prepared with the microfluidic process is shown in Figure 5. 14.

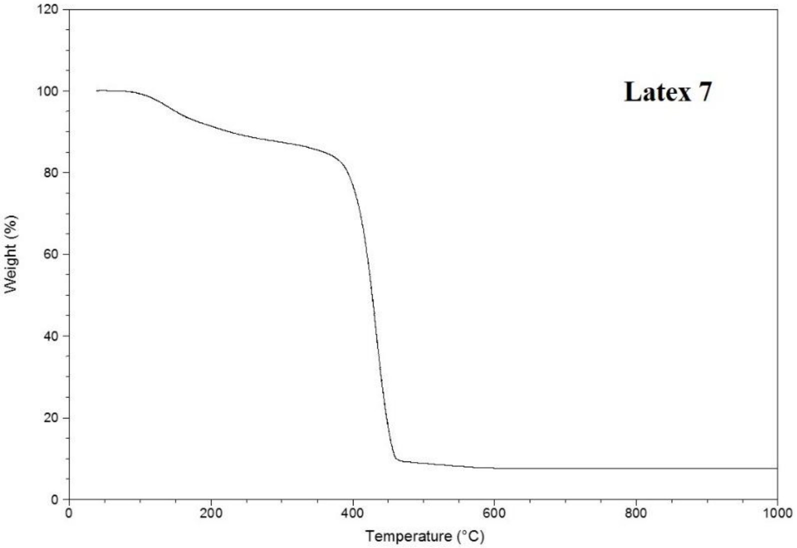

Figure 5. 14. Thermogravimetric curve of Latex 7.

The result is in good agreement with the one reported in Figure 5. 5. One step mass loss of 70% is detected between 400 and 460 °C

5.5 Magnetic analysis

The magnetic properties of the samples were characterized by measuring hysteresis loops with a Vibrating Sample Magnetometer at 300 K (for more details see Appendix V- Magnetic Measurements)

The magnetic hysteresis loops of samples Latex 3 and Latex 5 are shown in Figure 5. 15.

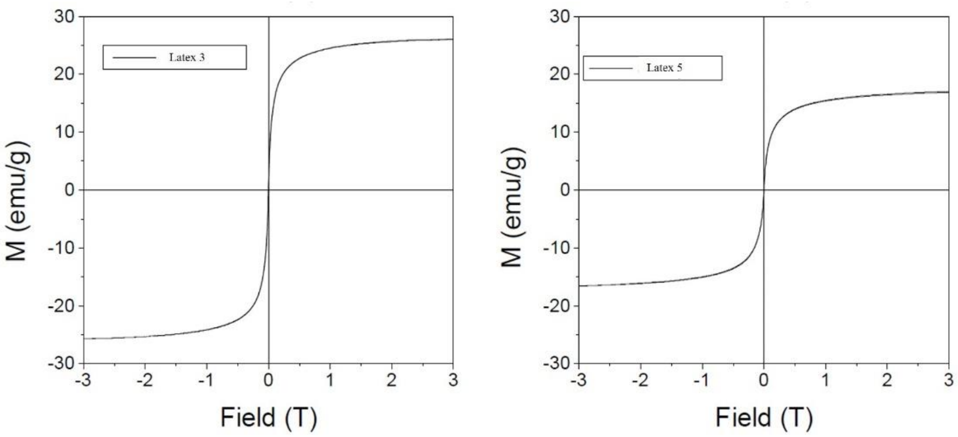

Figure 5. 15. Magnetization curves of magnetite/polystyrene nanoparticles at room temperature.

Neither remanence or coercivity was observed, indicating that the particles have some superparamagnetic properties. Indeed, the superparamagnetism enables the nanoparticles to respond to an applied magnetic field without any permanent magnetization. Under a large external magnetic field, the magnetization of the particles aligns with the field direction and reaches its saturation. The saturation magnetization of Latex 3 and Latex 5 were 17 emu/g and 26 emu/g, respectively. TGA was used to measure the weight contribution of magnetite nanoparticles in polymer matrix. The calculate magnetite content was 5.6% for Latex 5 and 14% for Latex 3.

5.5 Conclusions

Two methods, namely miniemulsion and microfluidic elongational-flow, were successfully developped to produce magnetic composite nanoparticles. We believe that the microprocess would be an interesting alternative to the conventional process with the additional advantage of using a quite smaller amount of reagents and less reaction time. TEM micrographs and EDX analyses revealed that magnetic nanoparticles were truly embedded in the polymeric matrix.

Future investigations will be performed to obtain a high homogeneity of the magnetite content in the polymeric nanoparticles. Also, future experiments have to measure the magnetic properties of all the samples. Finally, we will try to self-assembly the magnetic composite beads into a photonic crystals structure on the tip of a UV-Vis fiber optic. And we will monitor the optical response of these photonic crystals to external magnetic stimuli for the fabrication of a novel optical sensor.

6.

Conclusions and perspectives

6.1 Conlusions

The presented research work was carried out to develop composite nanospheres for new optical sensors.

In the first part, the state of the art of photonic crystal and in particular of responsive photonic crystal was presented and discussed.

In the second part of dissertation the development of optical sensors based on photonic crystals structure and its application to realize a humidity and a biological sensor was shown. In particular, the possibility to realize a photonic bandgap structure with commercial polystyrene nanoparticles involving a self-assembly of colloidal crystal directly on the fiber tip surface with very simple procedure was shown. In addition, the possible humidity sensing mechanisms was shown combining the properties of a polyacrylamide hydrogel and the photonic crystals structure on the fibre tip. In the Chapter 4, the development and the first sensing of a biological crystal colloidal was shown. Our UV-VIS fiber tip based nanochip provides a convenient, low-cost and label-free method for specific and highly sensitive detection of the biomolecular interactions.

In the Chapter 5 synthesis of magnetite composite nanoparticles with different technique were synthesized and morphology characterization was carried out.

The preliminary tests of the magnetic characterization of the as prepared samples show promising results. Moreover, by means of the microfluidic device it is possible to produce a good quality monodispersed composite polymeric nanoparticles.

6.2 Future perspectives

All results achieved during this work can surely be enhanced at different levels.

The self-assembly on the fiber optic tip could be enhanced by understanding and controlling defects that are observed in colloidal crystals and are classified under two categories, macro and micro. Macro defects are growth bands and cracks. Micro defects include vacancies and stacking faults. This is important for PBG materials application as defect control is the key to achieving useful optical devices.

For the fiber optic humidity sensor, the spectral response will be improved to change the specific morphology of the latex spheres. We have started to synthesized core-shell beads with a hydrophobic polystyrene core and hydrophilic PMMA-PAA shell for a more favorable permeation of the aqueous solution of acrylamide into the opal void due to the hydrogen bonding interactions between amide and carboxyl groups.

Future developments for the photonic crystal biosensors will be aim in test in diagnostics to provide the performance in biological fluids.

The magnetic photonic crystals should be characterized to enhance the superparamagnetic properties of composite latex and subsequently optical measurements will be made to prove the possibility to change the optical properties in response to an external magnetic field.

Scientific Production

Journal Articles

1) C. Taddei, S. Zuppolini, A. Borriello, M. Giordano. Bioinspired design of materials with magneto optic coupling for electromagnetic sensing. *XVIII AISEM 2015*, Trento, Italia 3–5 Febbraio 2015. (DOI:10.1109/AISEM.2015.7066846)

2) P. Di Palma, C. Taddei, A: Borriello, G. De Luca; A. Iadicicco, M. Giordano; S. Campopiano, L. Sansone. Self-assembled colloidal photonic crystal on the fiber optic tip as a sensing probe. IEEE Photonics Journal (2017) DOI: 10.1109/JPHOT.2017.2689075

3) L.Sansone, E. Macchia, C. Taddei, L. Torsi, M. Giordano. Label-free optical biosensing at sub-femtomolar detection limits. *To submitted*

Conferences, Workshops

1) E. Massera, L. Sansone, B. Alfano, T. Polichetti, M.L. Miglietta, A. Borriello, C. Taddei, M. Giordano, G. Di Francia. Optimization of interface for NO_2 not-heated sensing device based on RGO on chemically modified electrodes. *International Conference on Diamond and Carbon Materials*, Le Corum, Montpellier France, 4-8 September 2016

2) L. Sansone, M. Casalino, C. Taddei, M. Giordano. Graphene-Based Thermoelectric Generator. *International Conference GM-2016*, Paestum, Italia, 23-27 Maggio 2016

3) C. Taddei, S. Zuppolini, L. Sansone, A. Borriello, M. Giordano. Opaline polymeric film for humidity sensing *MiNaB-ICT: International Workshop on "Micro-Nano-Bio-ICT Convergence": Current Research and Future Trends,* Otranto, Italia, 13 – 15 Luglio 2015

4) C. Taddei, S. Zuppolini, A. Borriello, M. Giordano. Bioinspired design of materials with magneto optic coupling for electromagnetic sensing. *XVIII AISEM 2015,* Trento, Italia 3–5 Febbraio 2015.

7.

Appendix I - Characterization Techniques

This appendix serves to cover the theory behind some of the analytical techniques used in the work reported in this thesis. This will include how values are generated, the models that are employed in this process, what constitutes a reliable result, and the limitations of the techniques.

I. Scanning Electron Microscopy (SEM)

Optical microscopes have a resolution limited by the diffraction of the visible light source i.e. it is wavelength dependent. The minimum size feature that it can possibly resolve in normal transmission mode is ~ 200 nm with certain lenses and light sources.

Generally, if one wants to resolve colloidal particles and investigate their surface morphology on the submicron length scale, then scanning electron microscopy is used to image the sample. Instead of using a photon source, the SEM employs a tungsten filament and magnetic lenses to generate a focused beam of accelerated electrons, which have a much smaller wavelength than photons, and thus greater resolution capabilities. Practically the resolution of a SEM instrument is generally 1-20 nm and depends on the accelerating voltage used (typically 1-20 kV), with higher accelerating voltages giving greater resolution i.e. shorter electron wavelengths. However, radiation damage to the sample can be severe, particularly at higher accelerating voltages. Therefore, accelerating voltage must be carefully selected depending on the nature of the sample. Imaging is done under vacuum as the mean free path of electrons in air is very short. For this reason, the sample must not be damaged by vacuum conditions for successful analysis.

There are a number of electron-sample interactions that can arise. Signals that are used in imaging are typically secondary electrons and back-scattered electrons.

Samples for imaging must be electrically conducting and grounded in order to prevent electrostatic charge build-up. For this reason, non-conducting samples must be coated with a thin layer of carbon, gold, or platinum (amongst others) in a sputter chamber under vacuum.

All the samples were characterized by a ESEM-FEI Inspect-S, Electron Microscope coupled with Oxford INCA PentaFETx3 EDX spectrometer which is a Si(Li) detector, nitrogen cooled and equipped with an ultrathin window ATW2. Its resolution is of 137 eV at 5.9 keV (Mn Kα1). The results were processed by INCA software Energy.

Samples were prepared by drying the suspension of self organized colloidal structures at room temperature and coating with gold.

Advantages of SEM over TEM are that large areas of a sample can be imaged and analyzed via EDX. Disadvantages are that internal structure i.e. pores, cannot be resolved, and the resolution is lower than that of TEM.

EDX (Energy Dispersive X-ray Analysis) with the SEM is best for elemental mapping of samples.

When a sample is bombarded with electrons, it knocks off electrons from the inner shells of some atoms in the sample. Following this, higher energy electrons will move from an outer shell to fill the vacant position. In this process energy is released as an X-ray that is characteristic to both the element and the nature of the transition.

The detector converts the energy of the X-ray into an electrical voltage, that is then processed by the software. A plot of the intensity of a certain energy X-ray then allows one to determine the relative abundance of the elements in a sample, however resolution is limited to about 1% by mass of the sample, and some of the lighter elements are not possible to detect.

II. Transmission Electron Microscopy (TEM)

In TEM, electrons are detected by a CCD camera after passing through the sample, interacting with it on the way. Samples are mounted onto very thin grids, typically made of copper. Accelerating voltages are much higher (typically ~200 kV) than those used in SEM and consequently much greater resolution of the sample is possible. Assuming the sample is thin enough and not made of an electron dense material then internal structure of the sample can be analyzed, which is particularly useful for hollow colloids and those with pores. One of the disadvantages when compared to SEM is that information regarding surface morphology is difficult to obtain and it might not be possible to image dense or thick samples due to the electrons being fully adsorbed or back scattered before passing through to the detector.

All the samples were characterized by a TEM FEI Tecnai G12 Spirit Twin with emission source LaB6 (120 kV, spot size 1) and images were acquired by CCD camera Fei Eagle 4K. TEM specimens were prepared by dip coating the diluted solution onto a carbon-coated copper grid, dried in air and loaded into the electron microscope chamber.

III. Thermogravimetric Analysis (TGA)

TGA is a method in which changes in physical and chemical properties of materials are measured as a function of increasing temperature (with constant heating rate), or as a function of time (with constant temperature and/or constant mass loss). TGA is commonly used to determine selected characteristics of materials that exhibit either mass loss or gain due to decomposition, oxidation, or loss of volatiles (such as moisture).

In terms of apparatus, TGA relies on a high degree of precision in three measurements: mass change, temperature, and temperature change. Therefore, the basic instrumental requirements for TGA are a precision balance with a pan loaded with the sample, and a programmable furnace. The furnace can be programmed either for a constant heating rate, or for heating to acquire a constant mass loss with time. Regardless of the furnace programming, the sample is placed in a small, electrically heated furnace equipped with a thermocouple to monitor accurate measurements of the temperature by comparing its voltage output with that of the voltageversus-temperature table stored in the computer’s memory. A reference sample may be placed on another balance in a separate chamber. The atmosphere in the sample chamber may be purged with an inert gas to prevent oxidation or other undesired reactions.

The instrument used was a TA-Q5000 (TA Instruments Ltd, West Sussex, UK). The measurements were conducted at a heating rate of 20°C/min from 40 to 1000°C, using about 10.0 mg of the sample in platinum pan. The experiments were done under nitrogen atmosphere at flow rate of 20 mL/min.

IV. Optoelectronic Setup

The optoelectronic setup is schematically plotted in A. 1.

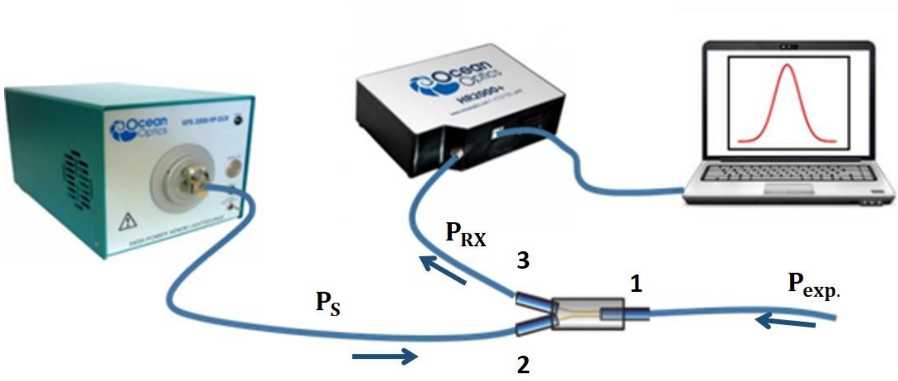

A. 1. Schematic view of optoelectronic set up.

Spectral reflectance measurements were carried out via a common configuration involving a lab-grade fiber splitter with the three ports connected to a xenon optical source (OceanOptics HPX-2000 185-2000nm), to the fiber probe, and to an optical spectrum analyzer (OceanOptics, HR 2000+).

The selected fibers (including the coupler) exhibit a 200 µm core and 240 µm cladding. The fiber tips were achieved by high precision fiber cleaver and their quality was controlled by microscope images.

In order to compare the experimental and numerical spectra, it is necessary to consider the power losses and the return power of the connectors in the experimental setup. In particular, every connector introduces an undesired reflected contribution that can cover the information contribution.

In our setup, the most critical unwanted reflected contribution is due to connector 1 because it is a direct power directly superimposed to the reflected probe power. Then the overall received power P_RX can be written as:

$$P_{RX} = \alpha P_S R_{exp} + \beta P_s \qquad \text{Equation A. 1}$$

where R_{exp} is the probe reflectance to be estimated and P_S is the source power, while α and β are the percentages of power probe and power source respectively in P_{RX}.

The spectra measured by the spectrometer, R_{meas}, can be written according to the following expression:

$$R_{meas} = \frac{P_{RX}-B}{P_{RX0}-B} \approx \frac{P_{RX}}{P_{RX0}} = \frac{\alpha P_S R_{exp} + \beta P_s}{\alpha P_S R_{\exp\_0} + \beta P_s} = \frac{\alpha R_{exp} + \beta}{\alpha\, R_{\exp\_0} + \beta} = \frac{R_{exp} + \gamma}{R_{\exp\_0} + \gamma}$$

Equation A. 2

where B is the dark power, P_{RX0} is the received reference power, R_{exp_0} the probe reference reflectance and $\gamma = \frac{\beta}{\alpha}$.

In our experiment, as reference has been chosen the air and consequently R_{exp_0}=0.034.

Inverting the equation A. 2, we obtain R_{exp} as:

$$R_{exp.} = R_{meas}\left(R_{exp\_0} + \gamma\right) - \gamma \qquad \text{Equation A. 3}$$

Thus, to estimate R_{exp} we evaluate the effects of the return loss, by calculating γ. This can be done with a preliminar optical configuration, characterized by R_{exp} equal to 0, by putting the bare fiber tip immersed in an index matching gel. With this configuration by using Equation A.3, we calculate γ according to the following equation:

$$0 = \bar{R}_{meas}\left(R_{\exp\_0} + \gamma\right) - \gamma \Leftrightarrow \gamma = \bar{R}_{meas}\left(R_{exp\_0} + \gamma\right) \Leftrightarrow$$

$$\gamma = \frac{\bar{R}_{meas} R_{\exp\_0}}{(1-\bar{R}_{meas})} \quad \text{Equation A. 4}$$

Once evaluated γ, we measure R_{meas} by using the spectrometer and estimate R_{exp} according to Equation A.2.

V Magnetic Measurements

The magnetic properties of the sample were obtained by using a vibrating sample magnetometer (VSM) operating at a vibration frequency of 55 Hz and at a fixed temperature of 300 K.

In a VSM, a sample is placed within suitably placed sensing coils, and is made to undergo sinusoidal motion, i.e., mechanically vibrated. If the sample is magnetic, this constant magnetic field will magnetize the sample by aligning the magnetic domains, or the individual magnetic spins, with the field. The stronger the constant field, the larger the magnetization will be. The magnetic dipole moment of the sample will create a magnetic field around the sample. As the sample is moved up and down. this magnetic stray field is changing as a function of time and can be sensed by a set of pick-up coils. The resulting magnetic flux changes induce a voltage in the sensing coils that is proportional to the magnetic moment of the sample

Variable temperatures may be achieved using either cryostats or furnace assemblies. In the context of the current discussion, we will consider electromagnet based systems only, as magnetic media are usually characterized at ambient temperature.

References

1. Yablonovitch, E. Inhibited spontaneous emission in solid-state physics and electronics. *Phys. Rev. Lett.* 58, 2059 (1987).

2. John, S. Strong localization of photons in certain disordered dielectric superlattices. *Phys. Rev. Lett.* 58, 2486 (1987).

3. Fink, Y., Urbas, A. M., Bawendi, M. G., Joannopoulos, J. D. & Thomas, E. L. Block copolymers as photonic bandgap materials. *J. Light. Technol.* 17, 1963–1969 (1999).

4. Urbas, A., Fink, Y. & Thomas, E. L. One-dimensionally periodic dielectric reflectors from self-assembled block copolymer-homopolymer blends. *Macromolecules* 32, 4748–4750 (1999).

5. Gates, B. & Xia, Y. Fabrication and characterization of chirped 3D photonic crystals. *Adv. Mater.* 12, 1329–1332 (2000).

6. Marlow, F., Sharifi, P., Brinkmann, R. & Mendive, C. Opals: status and prospects. *Angew. Chemie Int. Ed.* 48, 6212–6233 (2009).

7. Ge, J., Hu, Y. & Yin, Y. Highly Tunable Superparamagnetic Colloidal Photonic Crystals. *Angew. Chemie* 119, 7572–7575 (2007).

8. Ge, J., Hu, Y., Zhang, T., Huynh, T. & Yin, Y. Self-Assem**bly and Field-R**esponsive Optical Diffractions of Superparamagnetic Colloids. 3671–3680 (2008).

9. Bowen, W. R. & Sharif, A. O. Long-range electrostatic attraction between like-charge spheres in a charged pore. *Nature* 393, 663–665 (1998).

10. Danov, K. D., Pouligny, B. & Kralchevsky, P. A. Capillary forces between colloidal particles confined in a liquid film: the finite-meniscus problem. *Langmuir* 17, 6599–6609 (2001).

11. Dimitrov, A. S., Miwa, T. & Nagayama, K. A comparison between the optical properties of amorphous and crystalline monolayers of silica

particles. *Langmuir* 15, 5257–5264 (1999).

12. Wickman, H. H. & Korley, J. N. Colloid crystal self-organization and dynamics at the air/water interface. *Nature* 393, 445–447 (1998).
13. Deckman, H. W., Dunsmuir, J. H., Garoff, S., McHenry, J. A. & Peiffer, D. G. Macromolecular self-organized assemblies. *J. Vac. Sci. Technol. B* 6, 333–336 (1988).
14. Trau, M., Saville, D. A. & Aksay, I. A. Field-induced layering of colloidal crystals. *Science (80-.).* 272, 706 (1996).
15. Yeh, S.-R., Seul, M. & Shraiman, B. I. Assembly of ordered colloidal aggregrates by electric-field-induced fluid flow. (1997).
16. Solomentsev, Y., Böhmer, M. & Anderson, J. L. Particle clustering and pattern formation during electrophoretic deposition: a hydrodynamic model. *Langmuir* 13, 6058–6068 (1997).
17. Arora, A. K. & Tata, B. V. R. Interactions, structural ordering and phase transitions in colloidal dispersions. *Adv. Colloid Interface Sci.* 78, 49–97 (1998).
18. Jiang, P., Bertone, J. F., Hwang, K. S. & Colvin, V. L. Single-crystal colloidal multilayers of controlled thickness. *Chem. Mater.* 11, 2132–2140 (1999).
19. Hartsuiker, A. & Vos, W. L. Structural properties of opals grown with vertical controlled drying. *Langmuir* 24, 4670–4675 (2008).
20. Kuai, S.-L., Hu, X.-F., Hache, A. & Truong, V.-V. High-quality colloidal photonic crystals obtained by optimizing growth parameters in a vertical deposition technique. *J. Cryst. Growth* 267, 317–324 (2004).
21. McLachlan, M. A., Johnson, N. P., Richard, M. & McComb, D. W. Thin film photonic crystals: synthesis and characterisation. *J. Mater. Chem.* 14, 144–150 (2004).
22. Van Winkle, D. H. & Murray, C. A. Layering transitions in colloidal

crystals as observed by diffraction and direct-lattice imaging. *Phys. Rev. A* 34, 562 (1986).

23. Neser, S., Bechinger, C., Leiderer, P. & Palberg, T. Finite-size effects on the closest packing of hard spheres. *Phys. Rev. Lett.* 79, 2348 (1997).

24. Park, S. H., Qin, D. & Xia, Y. Crystallization of mesoscale particles over large areas. *Adv. Mater.* 10, 1028–1032 (1998).

25. Park, S. H. & Xia, Y. Assembly of mesoscale particles over large areas and its application in fabricating tunable optical filters. *Langmuir* 15, 266–273 (1999).

26. Gates, B., Qin, D. & Xia, Y. Assembly of nanoparticles into opaline structures over large areas. *Adv. Mater.* 11, 466–469 (1999).

27. Parker, A. R. *et al.* Bio-inspired variable structural color materials. *Chem. Soc. Rev.* 426, 786–787 (2012).

28. Parker, A. R., Welch, V. L., Driver, D. & Martini, N. Structural colour: opal analogue discovered in a weevil. *Nature* 426, 786–787 (2003).

29. Wang, H. & Zhang, K.-Q. Photonic crystal structures with tunable structure color as colorimetric sensors. *Sensors* 13, 4192–4213 (2013).

30. Fenzl, C., Hirsch, T. & Wolfbeis, O. S. Photonic crystals for chemical sensing and biosensing. *Angew. Chemie - Int. Ed.* 53, 3318–3335 (2014).

31. Weissman, J. M., Sunkara, H. B., Tse, A. S. & Asher, S. A. *Thermally Switchable Periodicities and Diffraction from Novel Mesoscopically Ordered Materials.* (DTIC Document, 1996).

32. Kumoda, M., Watanabe, M. & Takeoka, Y. Preparations and optical properties of ordered arrays of submicron gel particles: interconnected state and trapped state. *Langmuir* 22, 4403–4407 (2006).

33. Takeoka, Y. & Watanabe, M. Tuning structural color changes of porous thermosensitive gels through quantitative adjustment of the cross-linker in pre-gel solutions. *Langmuir* 19, 9104–9106 (2003).

References

34. Colodrero, S., Ocaña, M. & Míguez, H. Nanoparticle-based one-dimensional photonic crystals. *Langmuir* 24, 4430–4434 (2008).
35. Hawkeye, M. M. & Brett, M. J. Optimized Colorimetric Photonic-Crystal Humidity Sensor Fabricated Using Glancing Angle Deposition. *Adv. Funct. Mater.* 21, 3652–3658 (2011).
36. Tian, E. *et al.* Colorful humidity sensitive photonic crystal hydrogel. *J. Mater. Chem.* 18, 1116–1122 (2008).
37. Wang, Z. *et al.* Bioinspired Water-Vapor-Responsive Organic/Inorganic Hybrid One-Dimensional Photonic Crystals with Tunable Full-Color Stop Band. *Adv. Funct. Mater.* 20, 3784–3790 (2010).
38. Kim, E., Kim, S. Y., Jo, G., Kim, S. & Park, M. J. Colorimetric and resistive polymer electrolyte thin films for real-time humidity sensors. *ACS Appl. Mater. Interfaces* 4, 5179–5187 (2012).
39. Kang, Y., Walish, J. J., Gorishnyy, T. & Thomas, E. L. Broad-wavelength-range chemically tunable block-copolymer photonic gels. *Nat. Mater.* 6, 957–960 (2007).
40. Fudouzi, H. & Sawada, T. Photonic rubber sheets with tunable color by elastic deformation. *Langmuir* 22, 1365–1368 (2006).
41. Saado, Y., Golosovsky, M., Davidov, D. & Frenkel, A. Tunable photonic band gap in self-assembled clusters of floating magnetic particles. *Phys. Rev. B* 66, 195108 (2002).
42. Sacanna, S. & Philipse, A. P. Preparation and properties of monodisperse latex spheres with controlled magnetic moment for field-induced colloidal crystallization and (dipolar) chain formation. *Langmuir* 22, 10209–10216 (2006).
43. Xu, X., Friedman, G., Humfeld, K. D., Majetich, S. A. & Asher, S. A. Synthesis and utilization of monodisperse superparamagnetic colloidal particles for magnetically controllable photonic crystals. *Chem. Mater.* 14,

1249–1256 (2002).

44. Ge, J., Hu, Y., Biasini, M., Beyermann, W. P. & Yin, Y. Superparamagnetic magnetite colloidal nanocrystal clusters. *Angew. Chem. Int. Ed. Engl.* 46, 4342–5 (2007).
45. Ge, J. & Yin, Y. Magnetically responsive colloidal photonic crystals. *J. Mater. Chem.* 18, 5041 (2008).
46. Ge, J. *et al.* Magnetochromatic Microspheres : Rotating Photonic Crystals. 15687–15694 (2009).
47. Ge, J. & Yin, Y. Magnetically Tunable Colloidal Photonic Structures in Alkanol Solutions. *Adv. Mater.* 20, 3485–3491 (2008).
48. Zhao, Y., Zhao, X. & Gu, Z. Photonic crystals in bioassays. *Adv. Funct. Mater.* 20, 2970–2988 (2010).
49. Holtz, J. H. & Asher, S. A. Polymerized colloidal crystal hydrogel films as intelligent chemical sensing materials. *Nature* 389, 829–832 (1997).
50. Alexeev, V. L., Das, S., Finegold, D. N. & Asher, S. A. Photonic crystal glucose-sensing material for noninvasive monitoring of glucose in tear fluid. *Clin. Chem.* 50, 2353–2360 (2004).
51. Konopsky, V. N. & Alieva, E. V. Photonic crystal surface waves for optical biosensors. *Anal. Chem.* 79, 4729–4735 (2007).
52. Fang, Z., Chin, K., Qu, R. & Cai, H. *Fundamentals of optical fiber sensors*. 226, (John Wiley & Sons, 2012).
53. Udd, E. *Fiber optic sensors*. (Wiley Online Library, 1993).
54. Consales, M. *et al.* Lab-on-fiber technology: toward multifunctional optical nanoprobes. *ACS Nano* 6, 3163–3170 (2012).
55. Micco, A., Ricciardi, A., Pisco, M., La Ferrara, V. & Cusano, A. Optical fiber tip templating using direct focused ion beam milling. *Sci. Rep.* 5, (2015).
56. Ricciardi, A. *et al.* Lab-on-fiber technology: a new vision for chemical and

biological sensing. *Analyst* 140, 8068–8079 (2015).

57. Velev, O. D. & Kaler, E. W. Structured porous materials via colloidal crystal templating: from inorganic oxides to metals. *Adv. Mater.* 12, 531–534 (2000).
58. Petrušis, A., Rector, J. H., Smith, K., De Man, S. & Iannuzzi, D. The align-and-shine technique for series production of photolithography patterns on optical fibres. *J. Micromechanics Microengineering* 19, 47001 (2009).
59. Yan, H., Wang, M., Ge, Y. & Yu, P. Colloidal crystals self-assembled on the end face of fiber: Fabrication and characterizations. *Opt. Fiber Technol.* 15, 324–327 (2009).
60. Lin, Y., Zou, Y., Mo, Y., Guo, J. & Lindquist, R. G. E-beam patterned gold nanodot arrays on optical fiber tips for localized surface plasmon resonance biochemical sensing. *Sensors* 10, 9397–9406 (2010).
61. Lin, Y., Zou, Y. & Lindquist, R. G. A reflection-based localized surface plasmon resonance fiber-optic probe for biochemical sensing. *Biomed. Opt. Express* 2, 478–484 (2011).
62. Dhawan, A., Gerhold, M. D. & Muth, J. F. Plasmonic structures based on subwavelength apertures for chemical and biological sensing applications. *IEEE Sens. J.* 8, 942–950 (2008).
63. Dhawan, A. *et al.* Focused ion beam fabrication of metallic nanostructures on end faces of optical fibers for chemical sensing applications. *J. Vac. Sci. Technol. B* 26, 2168–2173 (2008).
64. Haibin, N., Ming, W., Wei, C. & Tingting, W. Assembly photonic crystal arrays on the facet of optical fibers and its applications. *2012 Photonics Glob. Conf. PGC 2012* (2012). doi:10.1109/PGC.2012.6458068
65. Pisco, M., Galeotti, F., Grisci, G., Quero, G. & Cusano, A. Self-assembled periodic patterns on the optical fiber tip by microsphere arrays. in *International Conference on Optical Fibre Sensors (OFS24)* 96341N–

96341N (International Society for Optics and Photonics, 2015).

66. Rowe-Taitt, C. A. *et al.* Array biosensor for detection of biohazards. *Biosens. Bioelectron.* 14, 785–794 (2000).
67. Moerner, W. E. New directions in single-molecule imaging and analysis. *Proc. Natl. Acad. Sci.* 104, 12596–12602 (2007).
68. Cox, W. G. & Singer, V. L. Fluorescent DNA hybridization probe preparation using amine modification and reactive dye coupling. *Biotechniques* 36, 114–123 (2004).
69. Cooper, M. A. Label-free screening of bio-molecular interactions. *Anal. Bioanal. Chem.* 377, 834–842 (2003).
70. Fang, Y., Ferrie, A. M., Fontaine, N. H., Mauro, J. & Balakrishnan, J. Resonant waveguide grating biosensor for living cell sensing. *Biophys. J.* 91, 1925–1940 (2006).
71. Skivesen, N. *et al.* Photonic-crystal waveguide biosensor. *Opt. Express* 15, 3169–3176 (2007).
72. Lin, B. *et al.* A label-free optical technique for detecting small molecule interactions. *Biosens. Bioelectron.* 17, 827–834 (2002).
73. White, I. M. & Fan, X. On the performance quantification of resonant refractive index sensors. *Opt. Express* 16, 1020–1028 (2008).
74. Mortensen, N. A., Xiao, S. & Pedersen, J. Liquid-infiltrated photonic crystals: enhanced light-matter interactions for lab-on-a-chip applications. *Microfluid. Nanofluidics* 4, 117–127 (2008).
75. Rindorf, L. & Bang, O. Highly sensitive refractometer with a photonic-crystal-fiber long-period grating. *Opt. Lett.* 33, 563–565 (2008).
76. Bruck, R., Melnik, E., Muellner, P., Hainberger, R. & Lämmerhofer, M. Integrated polymer-based Mach-Zehnder interferometer label-free streptavidin biosensor compatible with injection molding. *Biosens. Bioelectron.* 26, 3832–3837 (2011).

References

77. Voisin, V., Pilate, J., Damman, P., Mégret, P. & Caucheteur, C. Highly sensitive detection of molecular interactions with plasmonic optical fiber grating sensors. *Biosens. Bioelectron.* 51, 249–254 (2014).
78. Malitson, I. H. Interspecimen Comparison of the Refractive Index of Fused Silica. *J. Opt. Soc. Am.* 55, 1205 (1965).
79. Sultanova, N., Kasarova, S. & Nikolov, I. Dispersion properties of optical polymers. *Acta Phys. Pol. A* 116, 585–587 (2009).
80. Mıguez, H. *et al.* Photonic crystal properties of packed submicrometric SiO2 spheres. *Appl. Phys. Lett.* 71, 1148–1150 (1997).
81. Ricciardi, A. *et al.* Evidence of guided resonances in photonic quasicrystal slabs. *Phys. Rev. B* 84, 85135 (2011).
82. Fan, S. & Joannopoulos, J. D. Analysis of guided resonances in photonic crystal slabs. *Phys. Rev. B* 65, 235112 (2002).
83. Kim, S. *et al.* Optimization of emulsion polymerization for submicron-sized polymer colloids towards tunable synthetic opals. *Bull. Korean Chem. Soc* 31, 1891–1896 (2010).
84. Rosenblatt, D., Sharon, A. & Friesem, A. A. Resonant grating waveguide structures. *IEEE J. Quantum Electron.* 33, 2038–2059 (1997).
85. Pisco, M. *et al.* Miniaturized Sensing Probes Based on Metallic Dielectric Crystals Self-Assembled on Optical Fiber Tips. *ACS Photonics* 1, 917–927 (2014).
86. Ding, H. *et al.* Responsive Colloidal Crystal for Spectrometer Grating. *ACS Photonics* 1, 121–126 (2014).
87. Shin, J., Braun, P. V. & Lee, W. Fast response photonic crystal pH sensor based on templated photo-polymerized hydrogel inverse opal. *Sensors Actuators, B Chem.* 150, 183–190 (2010).
88. Waterhouse, G. I. N. & Waterland, M. R. Opal and inverse opal photonic crystals: fabrication and characterization. *Polyhedron* 26, 356–368 (2007).

References

89. Green, N. M. [5] Avidin and streptavidin. *Methods Enzymol.* 184, 51–67 (1990).

90. Hendrickson, W. A. *et al.* Crystal structure of core streptavidin determined from multiwavelength anomalous diffraction of synchrotron radiation. *Proc. Natl. Acad. Sci.* 86, 2190–2194 (1989).

91. Nakanishi, K., Sakiyama, T., Kumada, Y., Imamura, K. & Imanaka, H. Recent advances in controlled immobilization of proteins onto the surface of the solid substrate and its possible application to proteomics. *Curr. Proteomics* 5, 161–175 (2008).

92. Aquino, L. C. L., Miranda, E. A., Duarte, I. S., Rosa, P. T. V & Bueno, S. M. A. Adsorption of human immunoglobulin G onto ethacrylate and histidine-linked methacrylate. *Brazilian J. Chem. Eng.* 20, 251–262 (2003).

93. Yu, K., Fan, T., Lou, S. & Zhang, D. Biomimetic optical materials: Integration of nature's design for manipulation of light. *Prog. Mater. Sci.* 58, 825–873 (2013).

94. Parker, A. R., Welch, V. L., Driver, D. & Martini, N. Structural colour: opal analogue discovered in a weevil. *Nature* 426, 786–787 (2003).

95. Li, F., Josephson, D. P. & Stein, A. Colloidal assembly: the road from particles to colloidal molecules and crystals. *Angew. Chemie Int. Ed.* 50, 360–388 (2011).

96. Remington, J. P., Troy, D. B. & Beringer, P. *Remington: The science and practice of pharmacy*. 1, (Lippincott Williams & Wilkins, 2006).

97. Mason, T. G., Wilking, J. N., Meleson, K., Chang, C. B. & Graves, S. M. Nanoemulsions: formation, structure, and physical properties. *J. Phys. Condens. Matter* 18, R635 (2006).

98. Webster, A. J. & Cates, M. E. Osmotic stabilization of concentrated emulsions and foams. *Langmuir* 17, 595–608 (2001).

99. Ouzineb, K., Graillat, C. & McKenna, T. F. Study of compartmentalization

in the polymerization of miniemulsions of styrene and butyl methacrylate. *J. Appl. Polym. Sci.* 91, 115–124 (2004).

100. Tlusty, T. & Safran, S. A. Microemulsion networks: the onset of bicontinuity. *J. Phys. Condens. Matter* 12, A253 (2000).

101. Solans, C., Izquierdo, P., Nolla, J., Azemar, N. & Garcia-Celma, M. J. Nano-emulsions. *Curr. Opin. Colloid Interface Sci.* 10, 102–110 (2005).

102. Sajjadi, S. Nanoemulsion formation by phase inversion emulsification: on the nature of inversion. *Langmuir* 22, 5597–5603 (2006).

103. Souilem, I. *et al.* A Novel Low-Pressure Device for Production of Nanoemulsions. *Chem. Eng. Technol.* 35, 1692–1698 (2012).

104. Whitesides, G. M. The origins and the future of microfluidics. *Nature* 442, 368–373 (2006).

105. Terry, S. C., Jerman, J. H. & Angell, J. B. A gas chromatographic air analyzer fabricated on a silicon wafer. *IEEE Trans. Electron Devices* 26, 1880–1886 (1979).

106. Yu, W. *et al.* Development of an Elongational-Flow Microprocess for the Production of Size-Controlled Nanoemulsions: Batch Operation. *Macromol. React. Eng.* Macromol. React. Eng., DOI: 10.1002/mren.201600024..

107. Ramirez, L. P. & Landfester, K. Magnetic polystyrene nanoparticles with a high magnetite content obtained by miniemulsion processes. *Macromol. Chem. Phys.* 204, 22–31 (2003).

108. Montagne, F., Mondain-Monval, O., Pichot, C. & Elaïssari, A. Highly magnetic latexes from submicrometer oil in water ferrofluid emulsions. *J. Polym. Sci. Part A Polym. Chem.* 44, 2642–2656 (2006).